HAWAII GEOTHERMAL PROJECT

ENGINEERING PROGRAM

QUARTERLY REPORT No. 5

JANUARY 15, 1975

Prepared Under

NATIONAL SCIENCE FOUNDATION

RESEARCH GRANT NO. GI-38319

By

Hi Chang Chai
Bill Chen
Ping Cheng
James Chou
Deane Kihara
Kah Hie Lau
L. Stephen Lau
Patrick Takahashi
Paul Yuen

Hilo College
University of Hawaii
Hilo, Hawaii 96720

College of Engineering
University of Hawaii
Honolulu, Hawaii 96822

TABLE OF CONTENTS

HAWAII GEOTHERMAL PROJECT

ENGINEERING PROGRAM

QUARTERLY REPORT NO. 5

January 15, 1975

INTRODUCTION

The objectives of the Engineering Program are (1) applied research in problem areas related to the extraction of energy from geothermal resources, and (2) planning, design, and specification of a research-oriented, environmentally-acceptable geothermal power plant. Work is progressing on two tasks:

Task 3.1 Geothermal Reservoir Engineering
Task 3.6 Optimal Geothermal Plant Design

This report summarizes the timetable (A) for each task, the progress made to date (B), and the future work planned (C).

TASK 3.1 GEOTHERMAL RESERVOIR ENGINEERING

A. Timetable

1. Numerical Modelling of Geothermal Reservoirs

Investigators: P. Cheng, K. H. Lau, and L. S. Lau

December 31, 1974	1. Complete investigation of the effect of vertical heat source on the upwelling of the water table 2. Formulate finite element solution of free convection in a geothermal reservoir with irregular geometry 3. Complete the study of free convection at high Rayleigh number in confined geothermal reservoirs
May 31, 1975	1. Complete investigation of the effects of geothermal heating on Ghyben-Herzberg lens 2. Complete numerical solutions for heat transfer and fluid flow characteristics in an axisymmetric geothermal reservoir 3. Complete numerical solution of steady state pumping and reinjection in a confined geothermal reservoir
December 31, 1975	1. Complete numerical solution of steady state pumping and reinjection in unconfined geothermal reservoirs 2. Complete finite element solution of free convection in a two-dimensional geothermal reservoir with irregular geometry 3. Formulate problem of transient responses in geothermal reservoirs with pumping and reinjection

2. Well Test Analysis and Physical Modelling

Investigators: P. Takahashi, B. Chen, and L. S. Lau

December, 1974	1. Select hardware for well testing 2. Assess software for well testing 3. Initiate fabrication of preliminary physical model 4. Develop well test and analysis methodology in conjunction with Geophysics Drilling Program 5. Initiate computer program on well test analysis
May, 1975	1. Purchase hardware and select software for well testing (with Geophysics Program) 2. Initiate fabrication of full scale physical model 3. Assess methods for measurement and analysis of two-phase flow 4. Design Ghyben-Herzberg lens physical model 5. Develop computer program to combine type curve matching and mass/energy balance into a single predictive tool
September, 1975	1. Initiate laboratory simulation studies 2. Fabricate Ghyben-Herzberg lens physical model 3. Purchase equipment to interface the different physical models
December, 1975	1. Analyze laboratory simulation runs and correlate with computer model 2. Interface physical models into a general model of a geothermal field 3. Develop methods for two-phase flow measurement and analysis 4. Measure temperature, pressure and flow rate--both downhole and at wellhead 5. Analyze data
December, 1976	1. Complete analysis of geothermal well data 2. Predict geothermal field performance

TASK 3.1 GEOTHERMAL RESERVOIR ENGINEERING

B. Progress to Date

Research in geothermal reservoir engineering, Task 3.1, has continued in the areas of numerical modelling, well test analysis, and physical modelling.

1. Numerical Modelling of Geothermal Reservoirs

During the past three months, work has been performed on the following three problems:

a. The Effects of Dike Intrusion on the Upwelling of Water Table

The study on heat transfer and fluid flow characteristics in an unconfined geothermal reservoir with dike intrusion on the basis of the perturbation method has been completed. It has been found that (1) hot water at shallow depth is possible near a hot dike, (2) the existence of a hot dike will have a noticeable effect on the upwelling of water table, although an upwelling of 2000 ft above sea level appears to be unlikely, (3) for an unconfined reservoir with two hot dikes extending halfway into the reservoir, the dikes act as a complete barrier for the movement of ground water, thus sealing off the seepage from the ocean. The details of the analysis are described in Technical Report No. 7 [1]. A manuscript based on this work will be submitted for publication shortly.

b. Free Convection at High Rayleigh Number in Confined Geothermal Reservoirs

The problem of free convection at low Rayleigh numbers in unconfined geothermal reservoirs was studied by Cheng and Lau [2] using a perturbation technique. The work by Cheng and Lau [2] is therefore applicable only to reservoirs with low permeability. In the present study, we focus our attention to free convection at high Rayleigh number with application to reservoirs with high permeability.

It is found that temperature distribution in reservoirs with high permeability is dramatically different from those with low permeability due to the strong convective current. Of particular interest is the vertical temperature profiles showing a temperature reversal which bears a strong resemblance to the measurements taken by Dr. G. Keller on the Kilauea drill hole [3]. The results of this paper will have important implications on the selection of drill sites, and will aid in the correct physical interpretation of field data during geophysical exploration.

In the mathematical formulation of the problem, the following assumptions have been made:

1) The flow and temperature fields are steady.
2) The groundwater and the porous rock are in local thermodynamic equilibrium.
3) The temperature of the fluid is everywhere below boiling for the pressure at that depth.
4) Boussinesq approximation is employed.

The governing equations for the simultaneous heat and mass transfer in a saturated porous medium are the continuity equation, Darcy's Law, energy equation, and equation of state. In terms of dimensionless stream function ($\Psi = \frac{\mu\psi}{\rho_s ghK}$ where μ, the viscosity of the fluid, ρ_s, the density of the the fluid at some reference condition, g, the gravitational acceleration, h, the depth of the reservoir, and K, the permeability of the aquifer) and dimensionless temperature ($\theta \equiv \frac{T-T_s}{T_c-T_s}$ where T_s is the temperature at some reference condition and T_c is the maximum temperature at the impermeable surface), the resultant set of non-linear partial differential equations are of elliptic type that can be approximated by a set of non-linear, algebraic equations by the finite difference method. The parameters in the equations are the aspect ratio L, and the Rayleigh number Ra where $Ra \equiv K\rho_s gh\beta\frac{(T_c-T_s)}{\mu\alpha}$ with β and α denoting the coefficient of thermal expansion and the diffusivity of the saturated porous medium. To insure convergence at large Rayleigh numbers, the standard finite difference method is modified with the procedures discussed by Greenspan [4] to convert into a resultant set of diagonally dominant linear algebraic equations. Over-relaxation method is used to accelerate the iteration process. Numerical solutions are found to be convergent for all values of parameters involved.

Computations were carried out for L = 4 and for Ra from 0 to 2,000 with the following three different boundary conditions.

Case 1. Cylindrical and rectangular island aquifer with caprock temperature specified. Consider an island aquifer bounded by ocean on the sides, confined by caprock at the top, and heated by a horizontal impermeable

surface at the bottom (Fig. 3.1-1A). The temperature of the ocean and the caprock are given by $\theta_s = 0$ and $\theta_a = 0.02$, and that of the heated surface is given by

$$\theta = \exp\left[-\left(\frac{R}{0.5}\right)^2\right] \quad \text{for cylindrical reservoirs,}$$

and $$\theta = \exp\left[-\left(\frac{X}{0.5}\right)^2\right] \quad \text{for rectangular reservoirs,}$$

where R and X are dimensionless coordinates given by $R \equiv r/h$ and $X = x/h$.

Fig. 3.1-2 shows the convective pattern in a cylindrical aquifer for two values of Ra. In both of these figures, cold water moves inland along the lower portion of the aquifer and is gradually being heated by the impermeable surface. Near the point of maximum heating, the fluid rises all the way to the top. Since the aquifer is confined at the top, the warm water is spread around the caprock and is finally discharged to the ocean in the upper portion of the aquifer. A comparison of Figs. 3.1-2A and 3.1-2B shows that the convective cells in Fig. 3.1-2A are absent in Fig. 3.1-2B. The temperature contours in a cylindrical island aquifer are shown in Fig. 3.1-3. For small values of Ra (Ra = 50, for example), the temperature contours are similar to those by conduction. As the value of Ra is increased, temperature contours develop into mushroom shapes. The results have important implications on the selection of a drilling site. It indicates that for a reservoir at a large value of Ra and having a hot heat source, a large amount of hot water is indeed available at shallow depths. The effects of Ra on horizontal temperature distribution at Y = 0.2, 0.4, 0.6, and 0.8 are plotted in Fig. 3.1-4 where it is shown that the horizontal temperature distribution exhibits a bell shape with a maximum value at the center of the aquifer. The rate of increase in temperature in the region near the center is rapid for large Ra, indicating a boundary layer behavior. The same data for Fig. 3.1-4 is replotted in Fig. 3.1-5 to show the vertical temperature profiles in a cylindrical island aquifer. At the location directly above the heat source (R = 0), temperature increases rapidly from nearly zero at the caprock to almost unity at a small vertical distance from the caprock. The vertical temperature profile at R = 0 is dramatically different from the rest of the profiles which have a temperature reversal at a vertical distance not too far from the caprock. It is worth mentioning

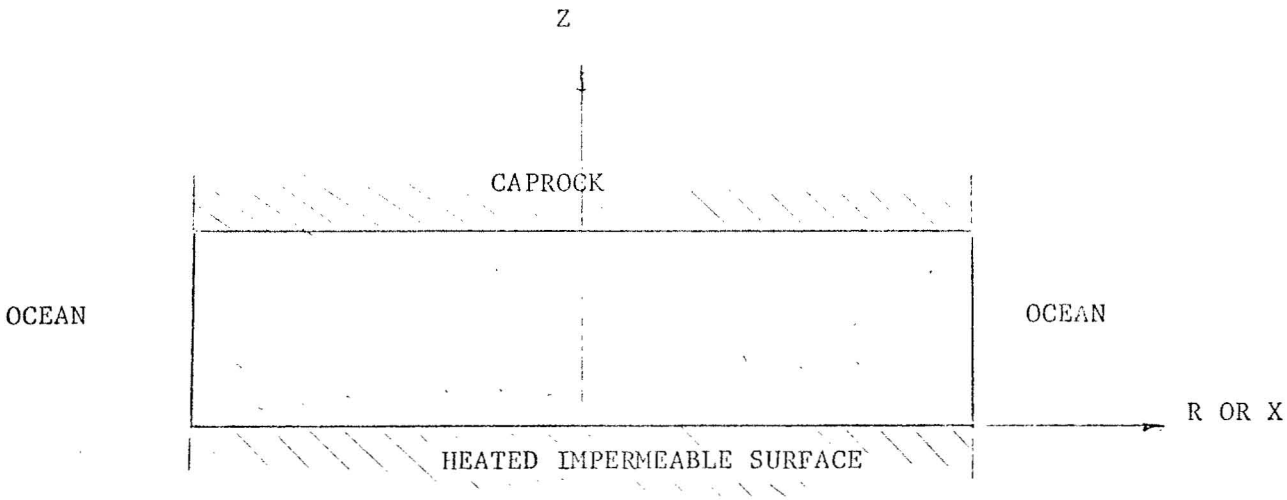

FIG. 3.1-1A ISLAND AQUIFER HEATED FROM BELOW

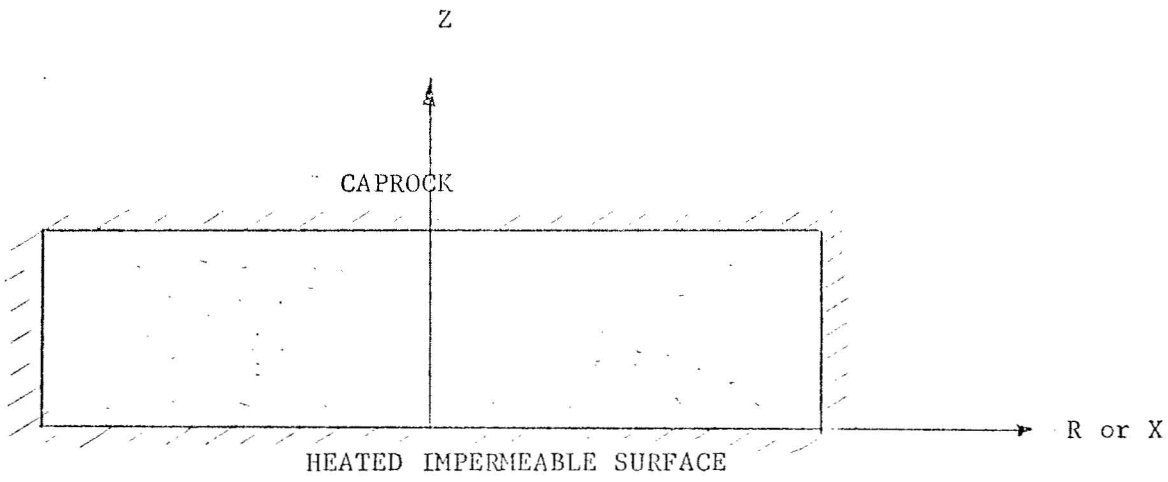

FIG. 3.1-1B BOUNDED AQUIFER HEATED FROM BELOW

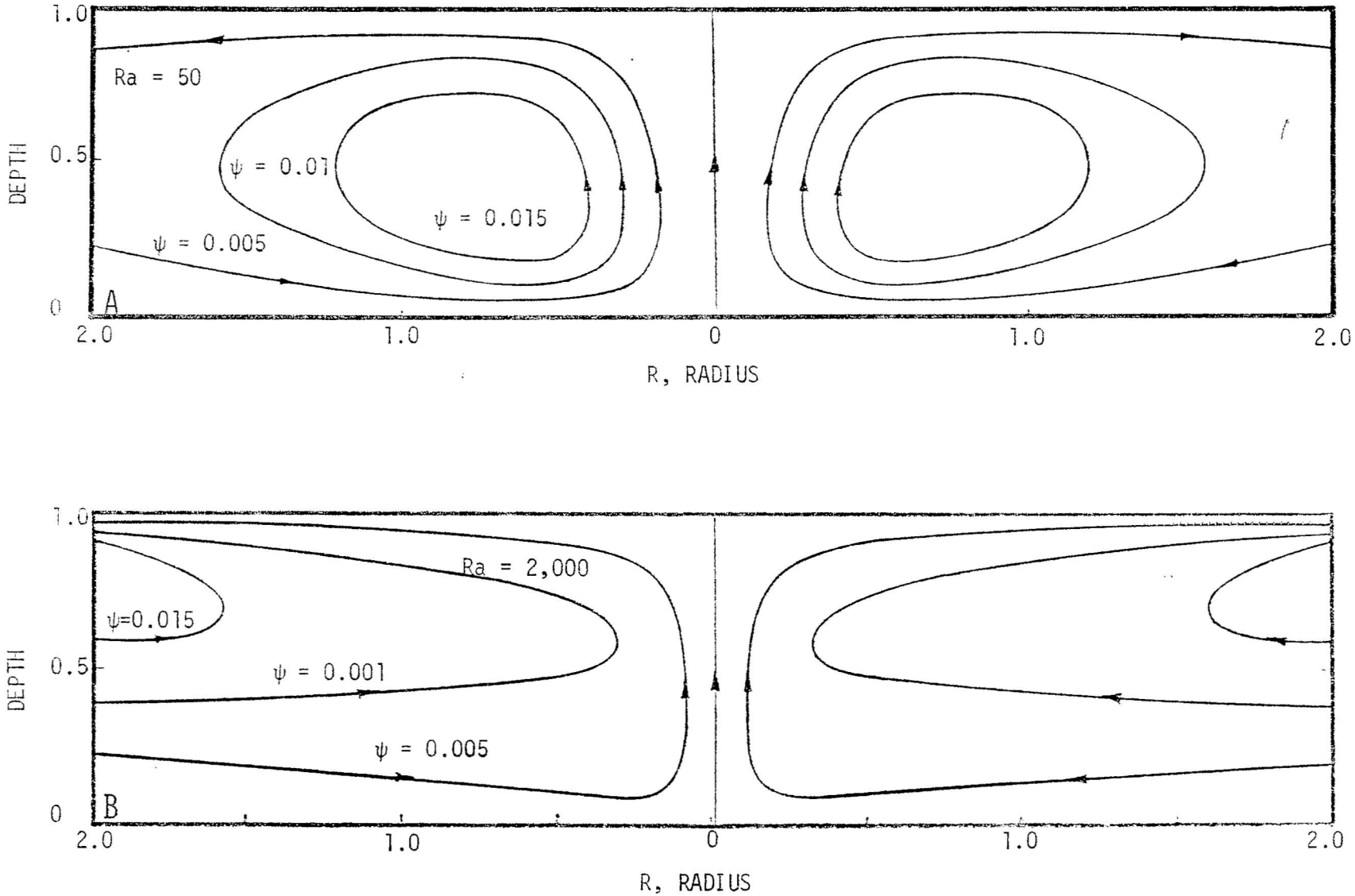

FIG. 3.1-2 STREAMLINES FOR A CYLINDRICAL ISLAND AQUIFER

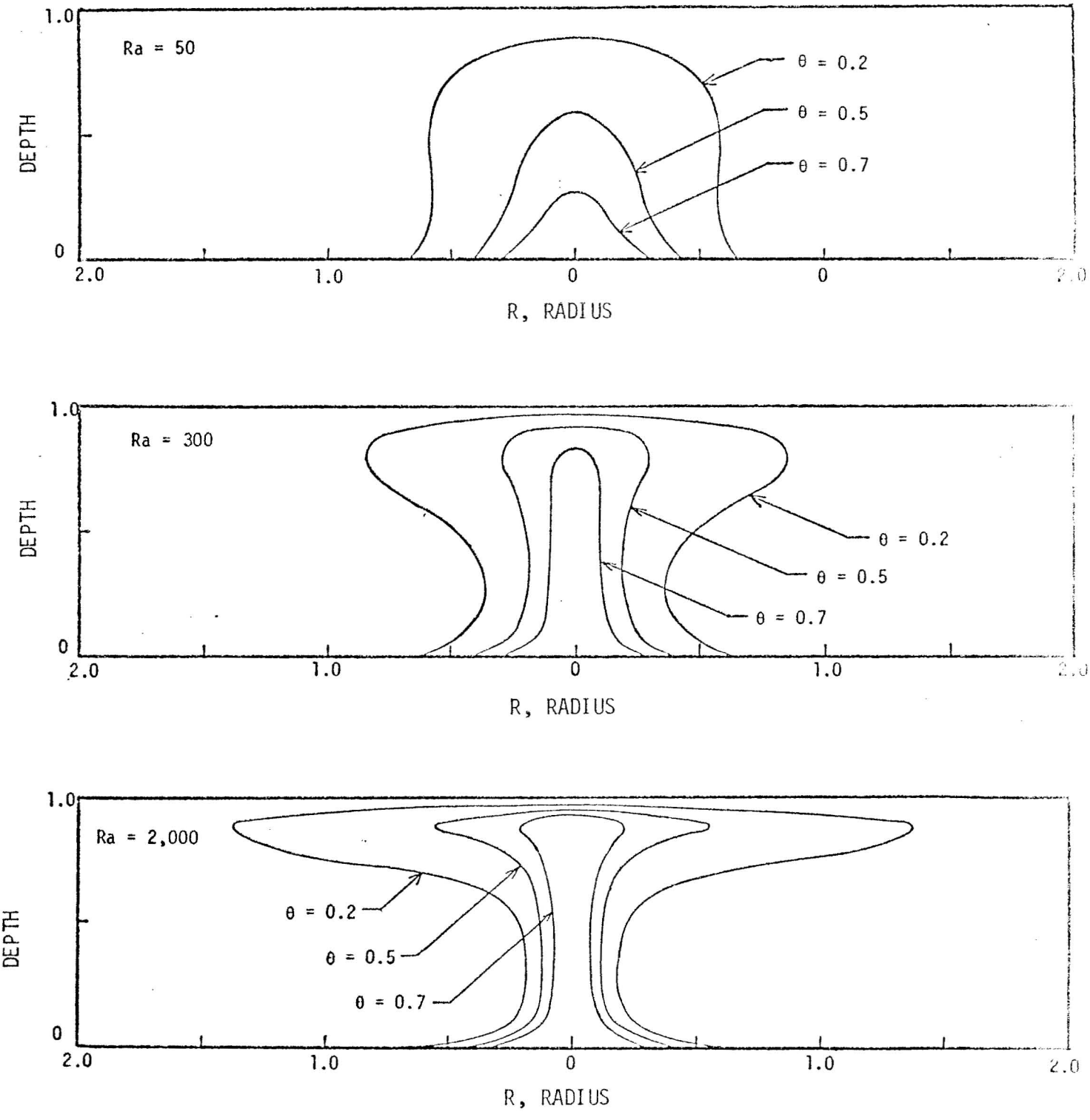

FIG. 3.1-3 TEMPERATURE CONTOURS IN A CYLINDRICAL ISLAND AQUIFER WITH CAPROCK TEMPERATURE SPECIFIED

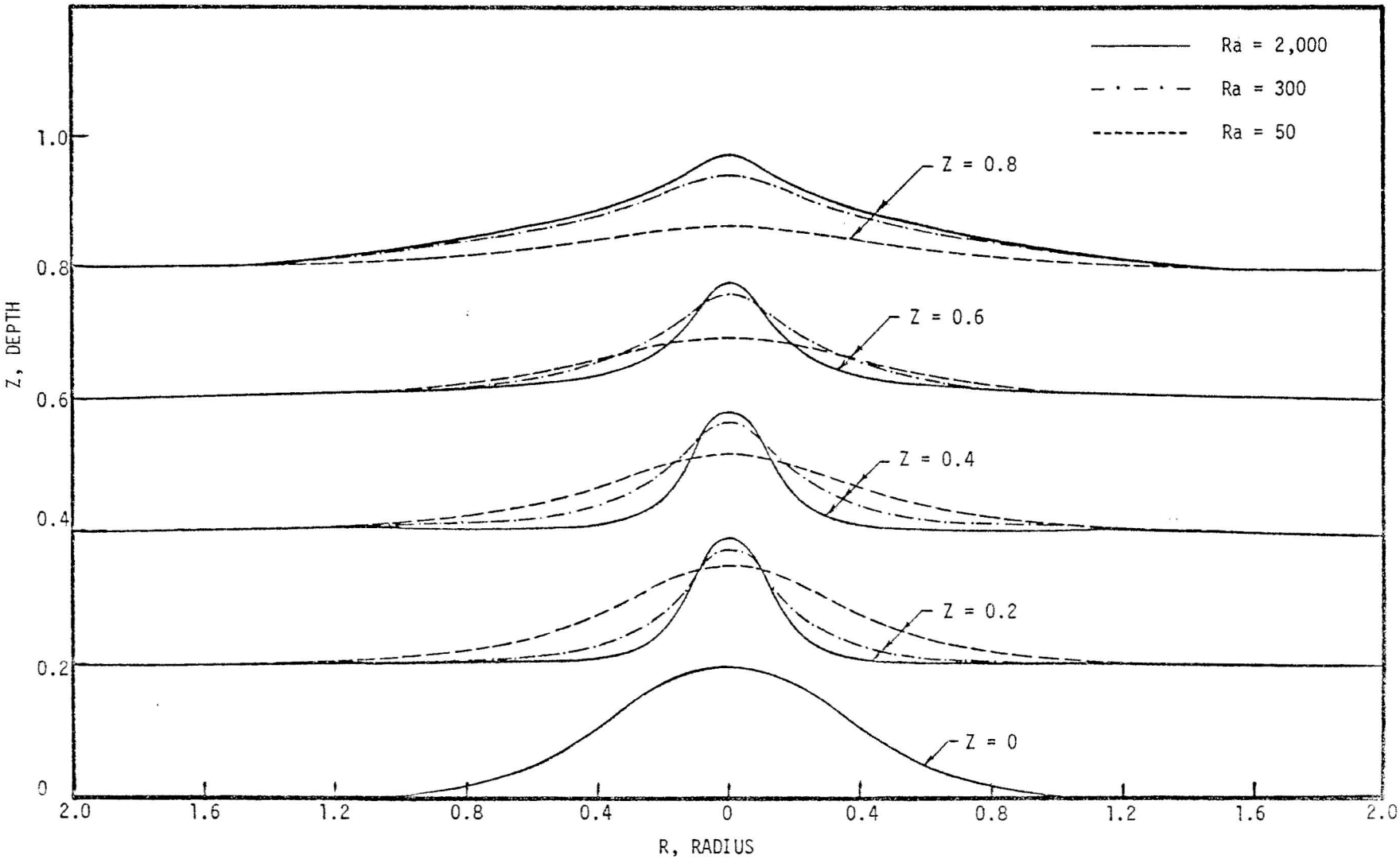

FIG. 3.1-4 HORIZONTAL TEMPERATURE DISTRIBUTION IN A CYLINDRICAL ISLAND AQUIFER WITH CAPROCK TEMPERATURE SPECIFIED

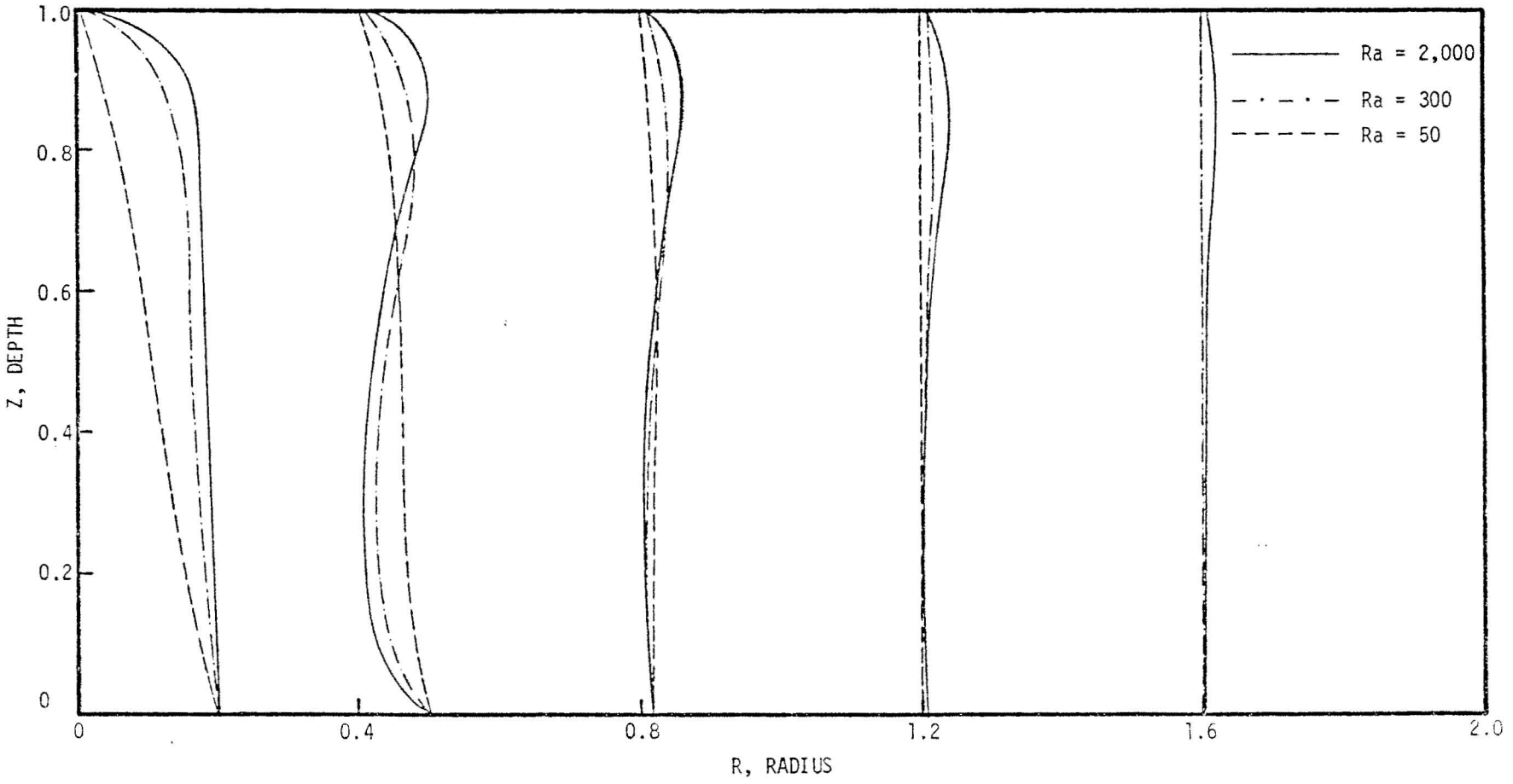

FIG. 3.1-5 VERTICAL TEMPERATURE PROFILES IN A CYLINDRICAL ISLAND AQUIFER WITH CAPROCK TEMPERATURE SPECIFIED

that the temperature reversal occurs because of the discharge of warm water toward the ocean. The behavior of temperature reversal is most pronounced for large Ra at a horizontal distance near the heat source. It is interesting to note that temperature vs. depth measurements obtained by G. Keller [3] show also a temperature reversal behavior (Fig. 3.1-6). A comparison between theory and measurements shows a striking similarity (Fig. 3.1-7), although the Island of Hawaii is supposed to be an unconfined aquifer. The comparison of temperature distribution between a cylindrical and a rectangular island aquifer with caprock temperature specified is shown in Figs. 3.1-8A and 3.1-8B. Here it is seen that temperature distribution in a cylindrical aquifer is everywhere below that of a rectangular aquifer because of the three-dimensional effect of the seepage.

Case 2. Cylindrical and rectangular island aquifer with nonheat conducting caprock. The geometry is similar to Case 1 except the thermal boundary condition of the caprock is changed to an adiabatic surface.

The convective pattern for a cylindrical island aquifer with nonheat conducting caprock is very similar to Fig. 3.1-2. The corresponding temperature contours are plotted in Fig. 3.1-9. A comparison of Fig. 3.1-9 and Fig. 3.1-3 shows that a substantially larger amount of hot water at shallow depth is available for Case 2 because of the nonheat conducting caprock. The data for Fig. 3.1-9 is replotted in Figs. 3.1-10 and 3.1-11 to show the effect of Ra on the horizontal and vertical temperature distribution. Again, the boundary layer behavior is pronounced for large Ra. As in Case 1, temperature distribution in a cylindrical island aquifer is everywhere lower than that in a rectangular island aquifer (Figs. 3.1-12A and 3.1-12B).

Effects of thermal boundary conditions on the caprock can be shown by comparing Case 1 and Case 2, as is shown in Figs. 3.1-13A and 3.1-13B. As is expected, temperature distribution everywhere in the reservoir with a nonheat conducting caprock is higher than that of a heat conducting caprock. However, the increase in temperature is most significant in the region adjacent to the caprock. The larger the value of Ra, the smaller the region in which temperature is affected. In other words, for large value of Ra, the effect of thermal boundary condition on the caprock would influence temperature distribution in a small region adjacent to the caprock; for the temperature distribution in the rest of the reservoir it is unaffected by the thermal condition at the caprock.

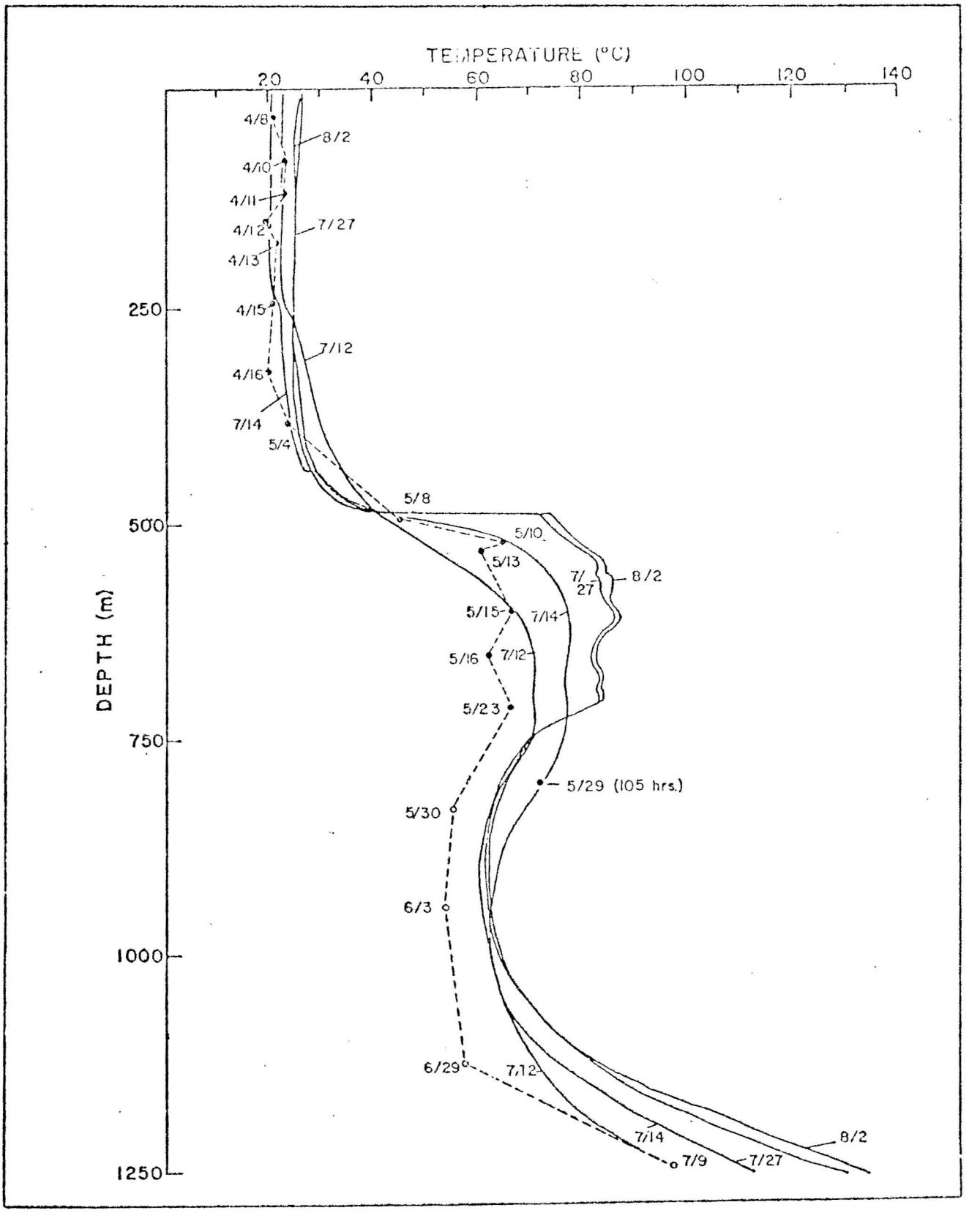

FIG. 3.1-6 TEMPERATURE PROFILES IN THE KILAUEA DRILL HOLE MEASURED BY KELLER

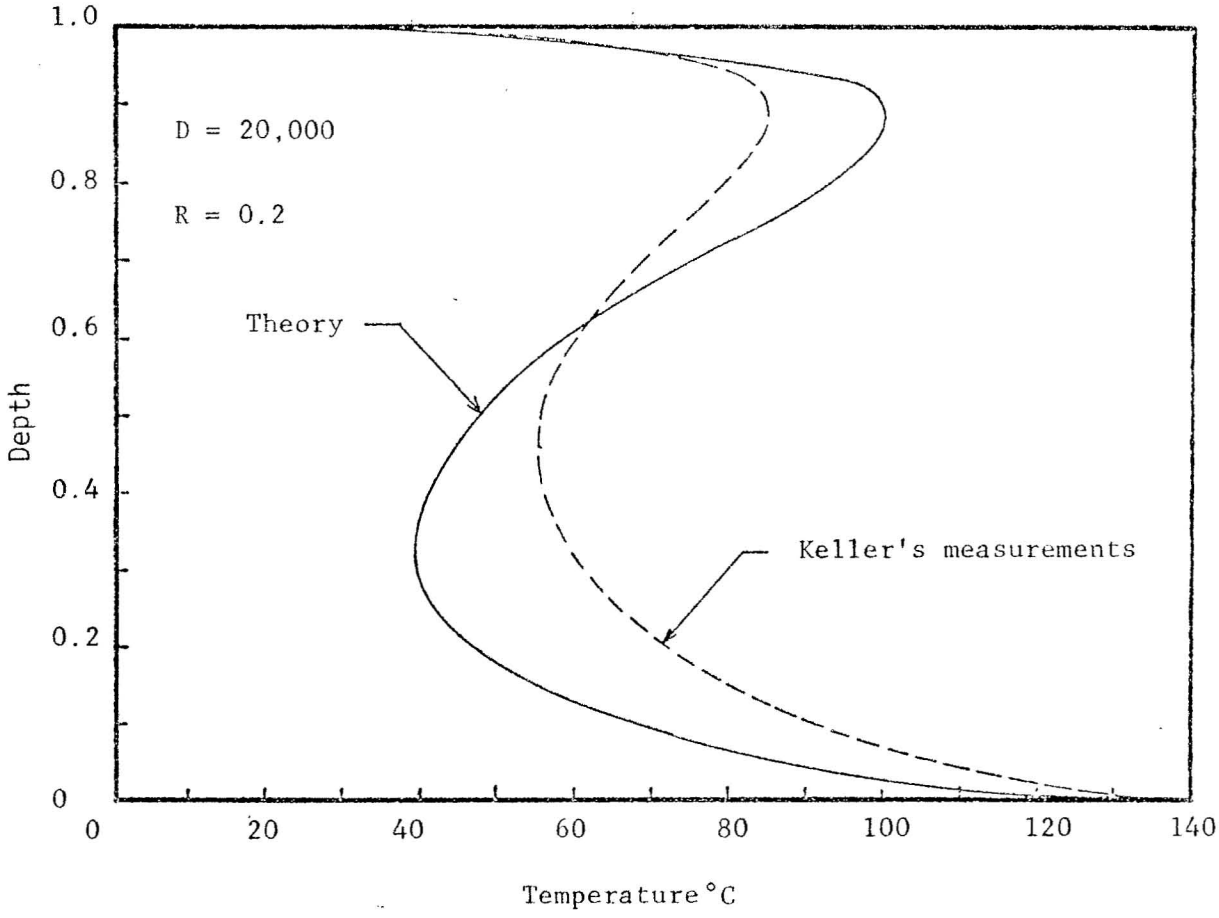

FIG. 3.1-7 COMPARISON OF THEORY AND MEASUREMENTS

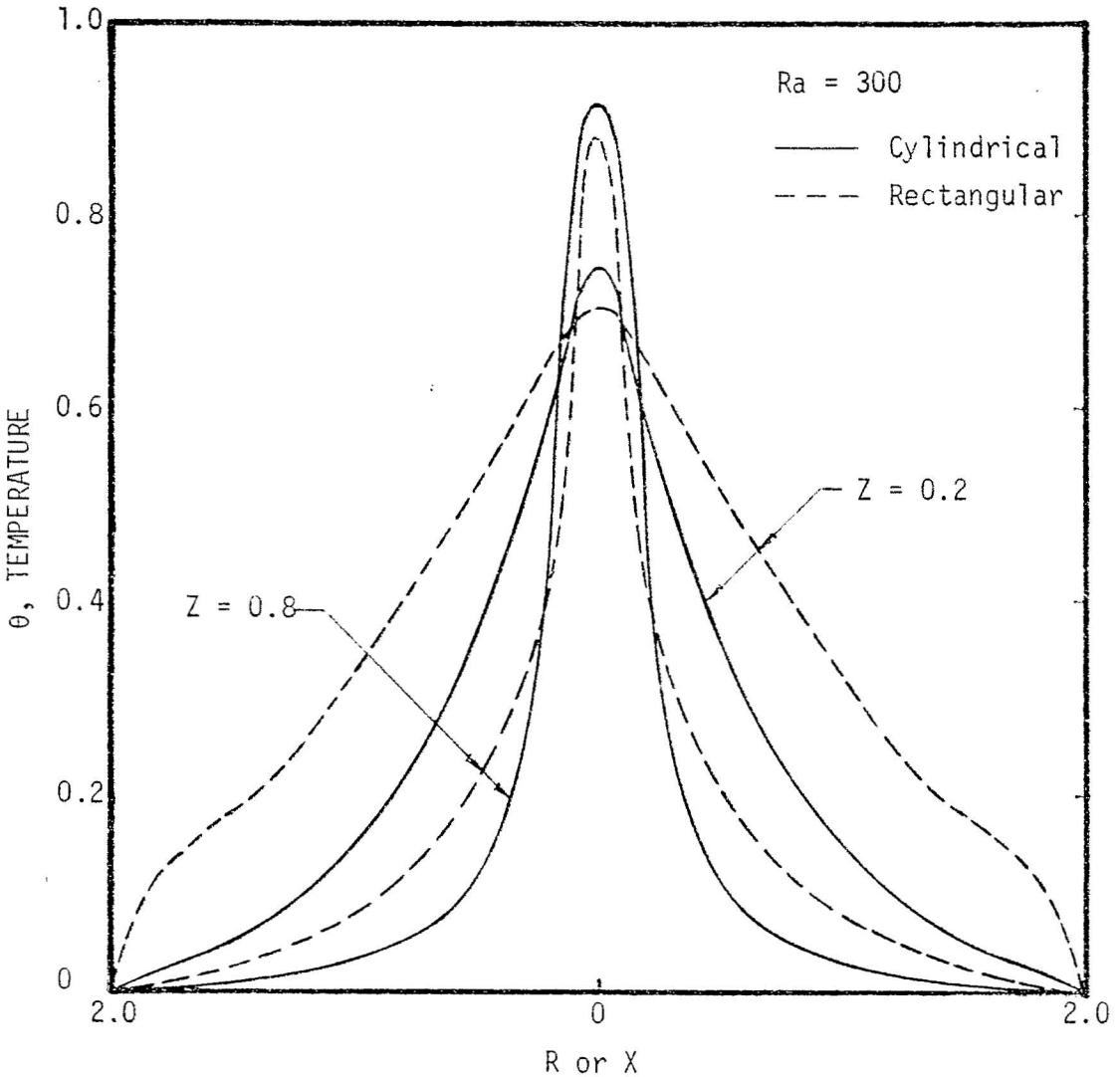

FIG. 3.1-8A COMPARISON OF HORIZONTAL TEMPERATURE DISTRIBUTION IN A CYLINDRICAL AND A RECTANGULAR ISLAND AQUIFER WITH CAPROCK TEMPERATURE SPECIFIED

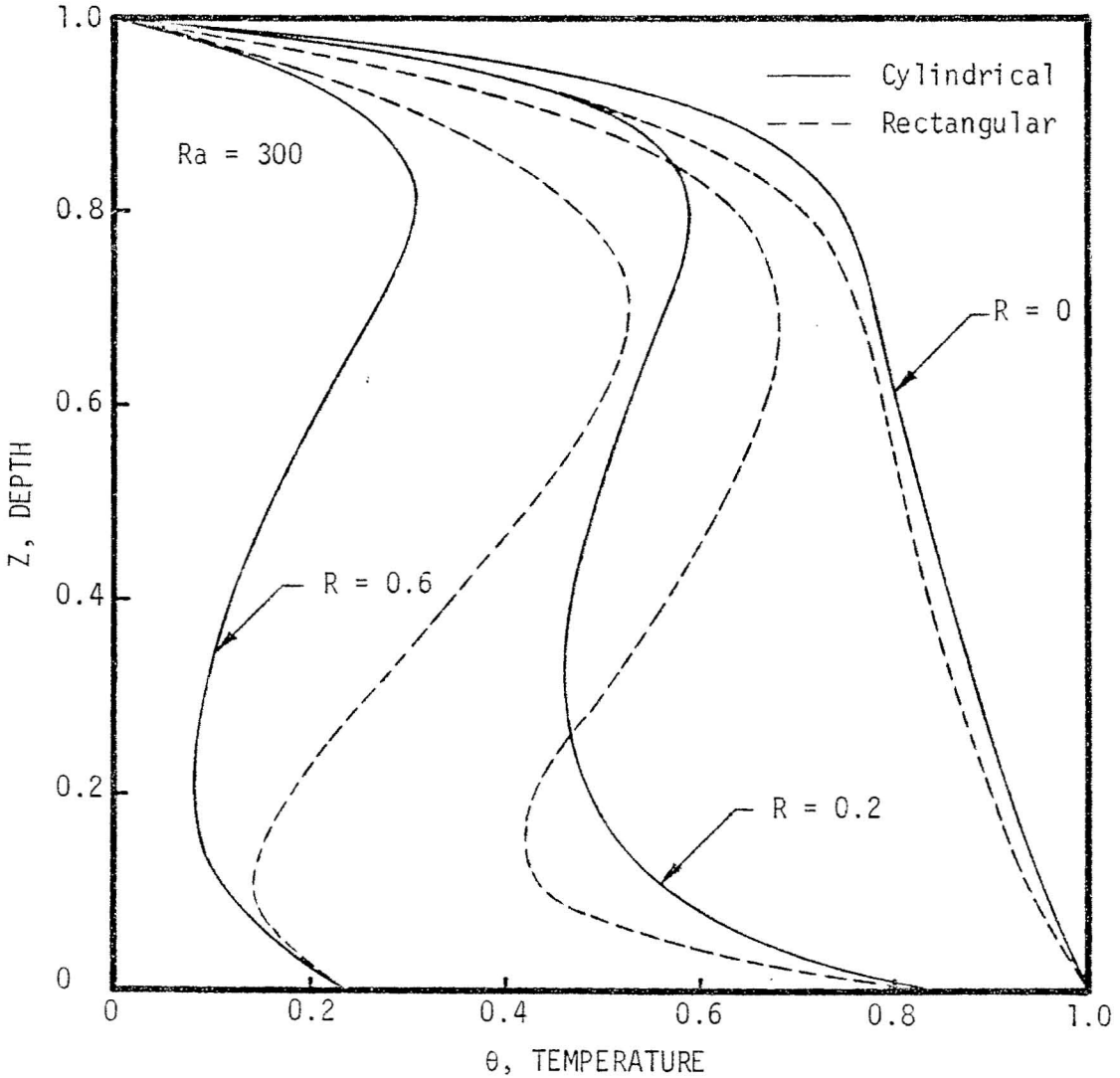

FIG. 3.1-8B COMPARISON OF VERTICAL TEMPERATURE PROFILES IN A CYLINDRICAL AND A RECTANGULAR ISLAND AQUIFER WITH CAPROCK TEMPERATURE SPECIFIED

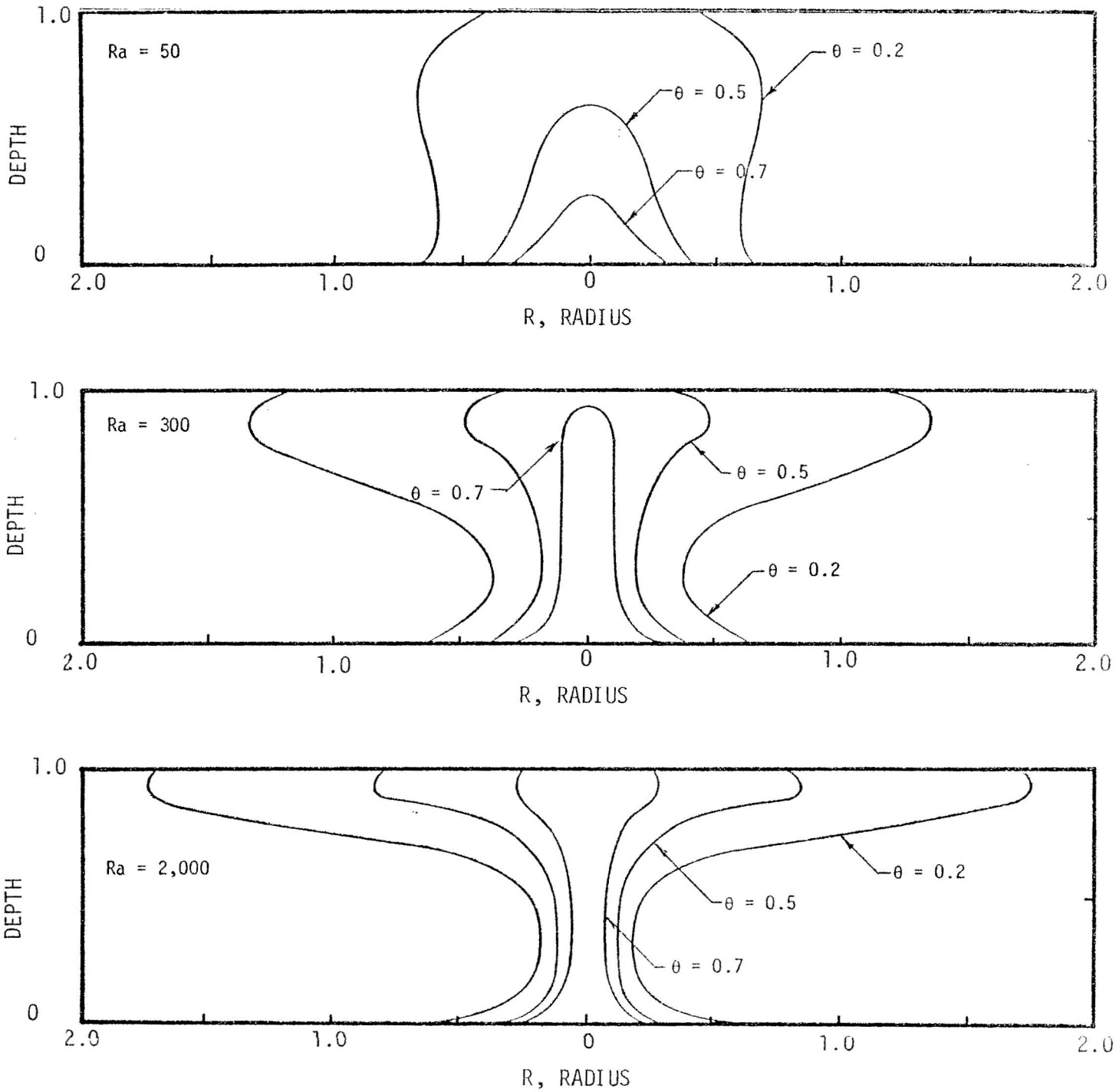

FIG. 3.1-9 TEMPERATURE CONTOURS IN A CYLINDRICAL ISLAND AQUIFER WITH ADIABATIC CAPROCK

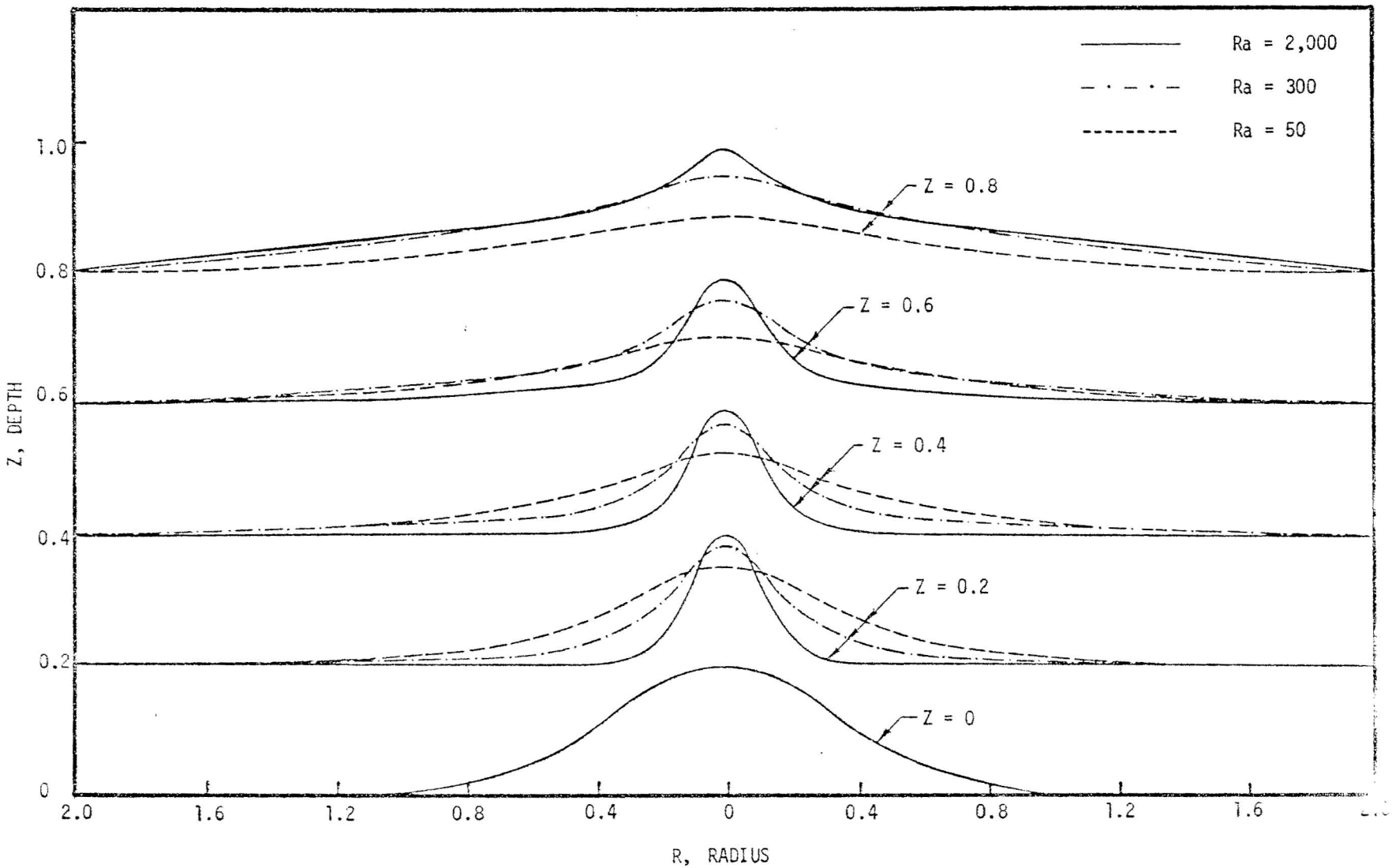

FIG. 3.1-10 HORIZONTAL TEMPERATURE DISTRIBUTION IN A CYLINDRICAL ISLAND AQUIFER WITH NON-HEAT CONDUCTING CAPROCK

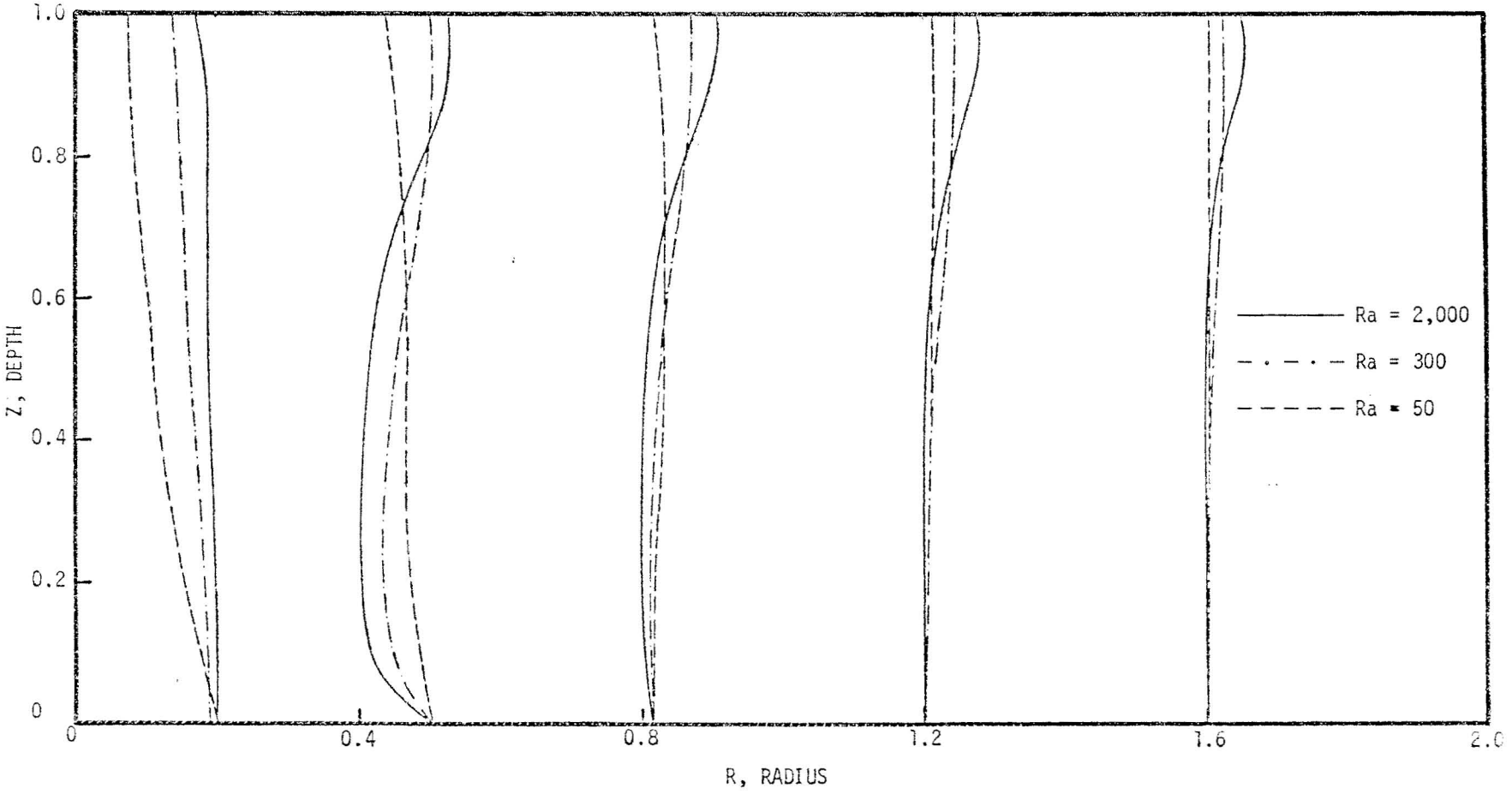

FIG. 3.1-11 VERTICAL TEMPERATURE PROFILES IN A CYLINDRICAL ISLAND AQUIFER WITH NON-HEAT CONDUCTING CAPROCK

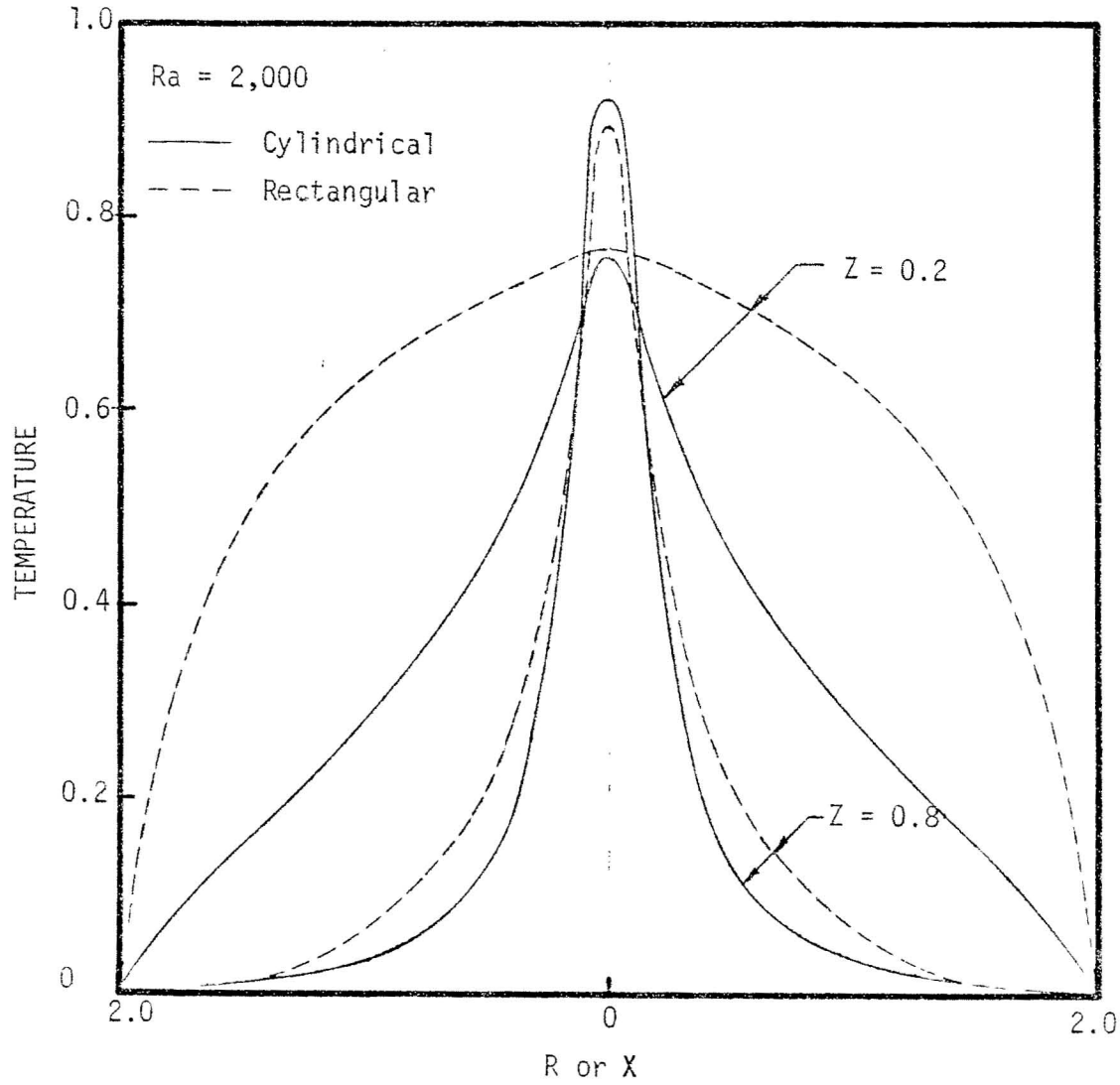

FIG. 3.1-12A COMPARISON OF HORIZONTAL TEMPERATURE DISTRIBUTION IN A CYLINDRICAL AND A RECTANGULAR ISLAND AQUIFER WITH ADIABATIC CAPROCK

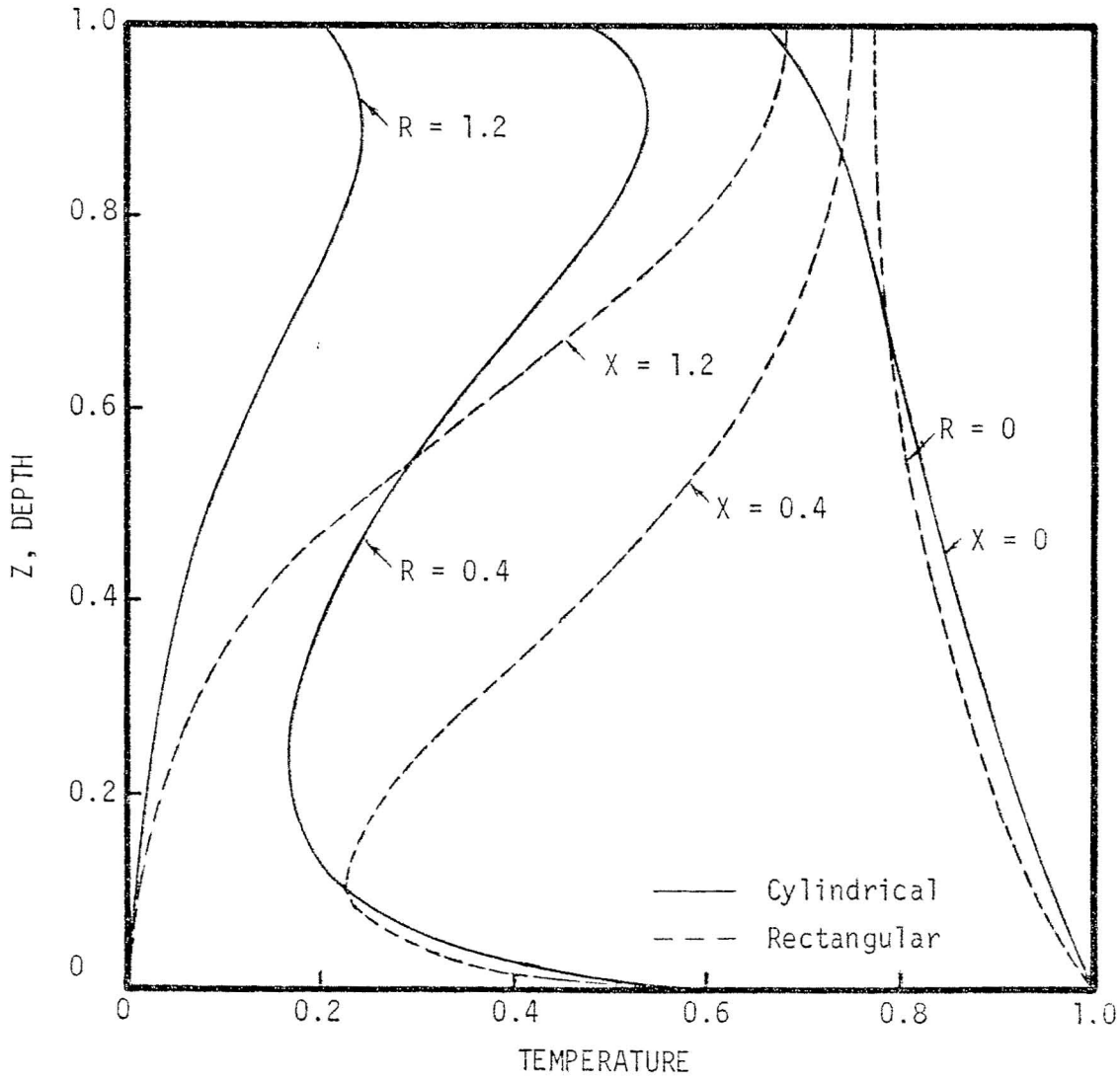

FIG. 3.1-12B COMPARISON OF VERTICAL TEMPERATURE PROFILES IN A CYLINCRICAL AND A RECTANGULAR ISLAND AQUIFER WITH ADIABATIC CAPROCK

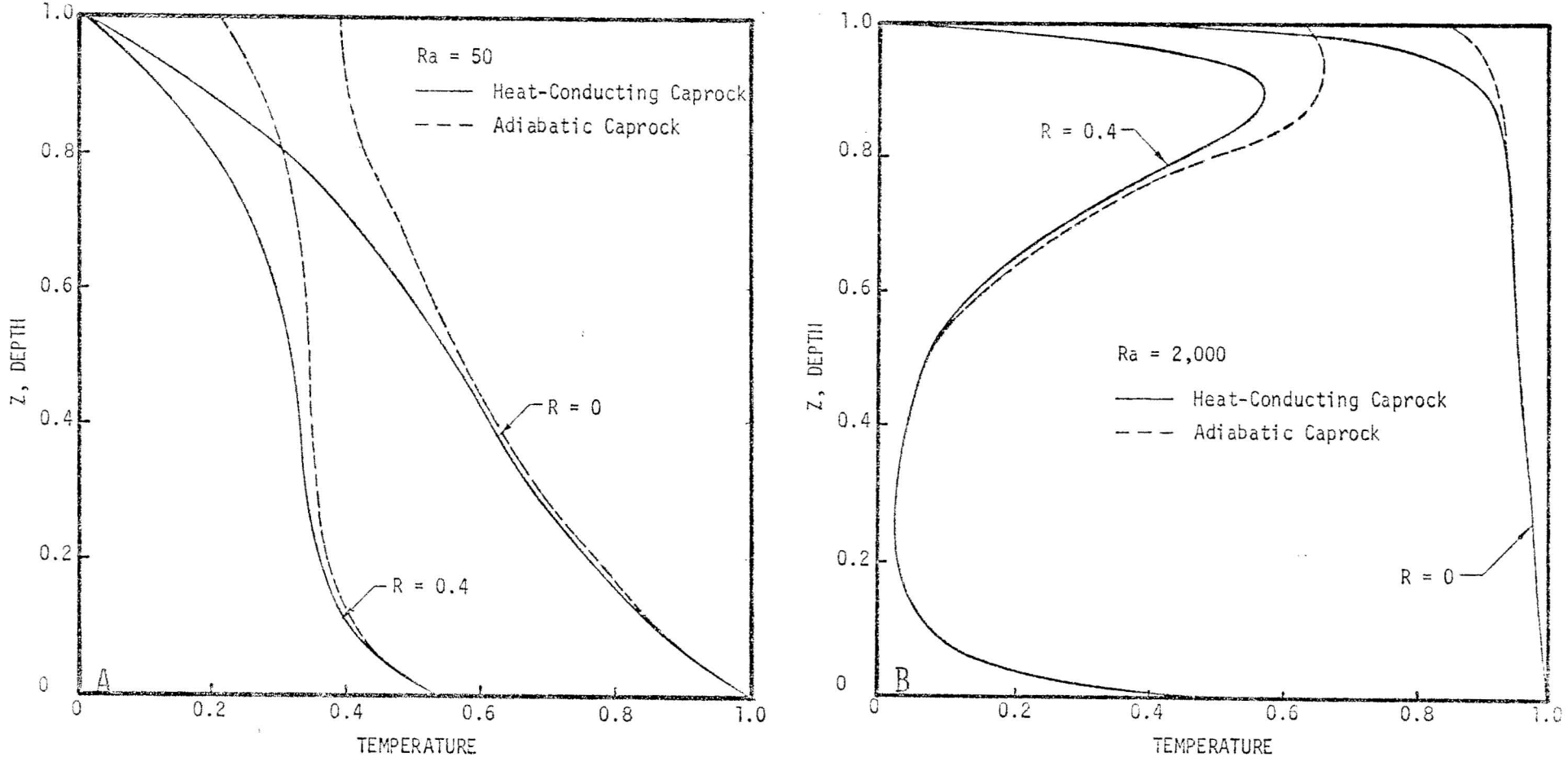

FIG. 3.1-13 EFFECT OF THERMAL BOUNDARY CONDITION OF THE CAPROCK ON THE VERTICAL TEMPERATURE PROFILES IN A CYLINDRICAL ISLAND AQUIFER

Case 3. Cylindrical and rectangular island aquifers with caprock temperatures specified. The geometry of this case is shown in Fig. 3.1-13 where the reservoir is bounded by impermeable surfaces. Temperature on the bottom impermeable surface is similar to Case 1. Temperatures on the rest of the impermeable surfaces are at zero.

The convective pattern for a cylindrical bounded aquifer with zero temperatures on the top and on the sides and heated from below is shown in Fig. 3.1-14. Here it is shown that two convective cells exist on either side of the heat source. Temperature distribution for this case is very similar to that of Case 1.

A manuscript covering this work is now under preparation for publication.

c. Steady Withdrawal and Reinjection of Fluids in a Confined Reservoir

The debugging of the computer program for the problem of steady withdrawal and reinjection of fluids in a confined rectangular reservoir has just been completed. We are now extending this work to the case of a cylindrical reservoir. The results of this work will be described in the next quarterly report.

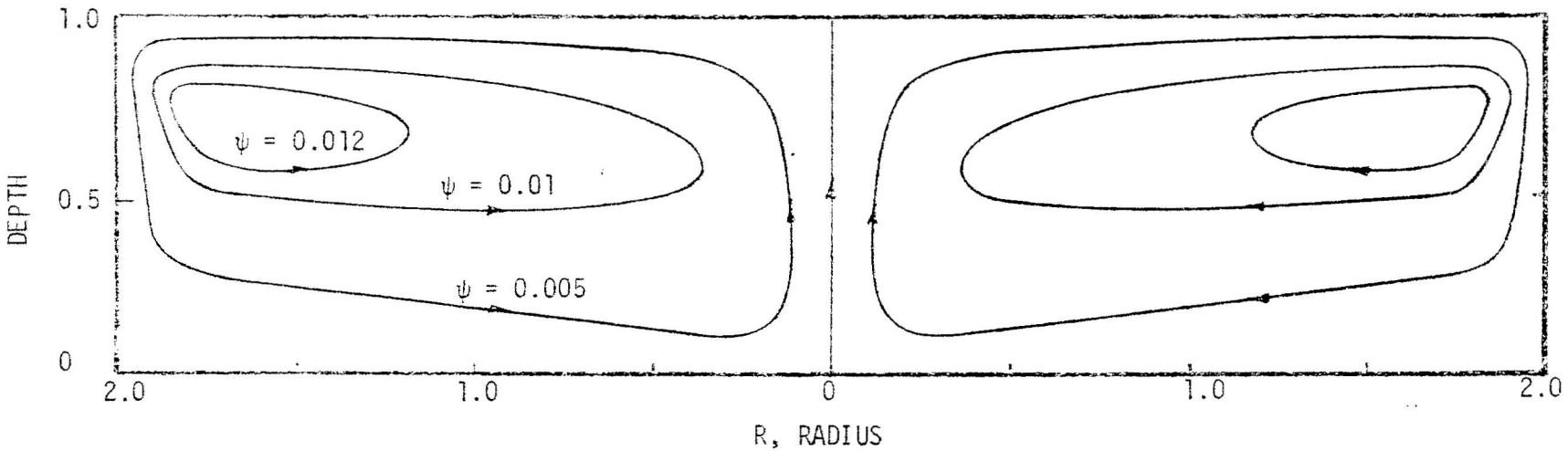

FIG. 3.1-14 STREAMLINES FOR A BOUNDED CYLINDRICAL RESERVOIR

2. Well Test Analysis and Physical Modelling

Geothermal reservoir engineering begins with exploration and progresses through stages of drilling, well testing, analysis and performance prediction. Investigators in the engineering phase of the program have worked closely with the geophysical effort in activities that impact engineering. The "well test analysis and physical modelling" team has progressed in three well-defined but closely interrelated, sequential and parallel areas. Close to completion is a master's thesis on formation evaluation, the interface region connecting geophysics and engineering. This initial probe has categorized the various techniques utilized in geophysical exploratory programs, especially with respect to engineering relevant data. All activities in the region of the geothermal well, from speculations into most probable reservoir configurations to fluid flow properties in the well itself, to measurement of the necessary parameters, have been considered. Study #2, well test analysis, logically extends the first. Methods used by the petroleum industry have been studied for adaptation to geothermal fluids. A third ongoing study involves physical modelling. The ultimate objective is the simulation of reservoir conditions so that, as in the second study, performance prediction can be achieved.

a. Formation Evaluation

The proper interpretation of data from well tests will determine the feasibility of utilizing a geothermal well. Both open-hole non-flowing and cased-hole production tests are used to aid in characterizing a reservoir. The required data includes formation thickness, permeability, porosity, water saturation, viscosity, compressibility, fluid and rock density, temperature and formation fluid pressures. The values for these parameters can be obtained in different ways depending upon the developmental phase of the well. For practical purposes, it is important to understand the ways in which these values are obtained.

The most common parameters calculated in formation evaluation are porosity, water saturation and permeability. The equations used below have been developed mainly for oil-field interpretation where NaCl is generally the dominant salt in the solution. As it is assumed that the formation fluid on the Island of Hawaii is brackish, these equations should be valid.

Water saturation, S_w, in terms of resistivities can be expressed by the Archie [5] formula, as

$$S_w = \frac{R_i/R_t}{R_z/R_w} \qquad (1)$$

where R_t is obtained from a deep-investigation device such as a lateral log; R_i is taken as the resistivity from a shallow-investigation device such as an induction log; R_w is taken as the resistivity from a spontaneous potential device and R_z is equal to $\frac{R_w R_{mf}}{ZR_{mf} + (1-Z)R_w}$. R_{mf} is obtained from a regular induction tool. Z is the fraction of invaded zone pore water that is formation water, and 1-Z is the fraction that is mud filtrate. For normal cases of invasion Z is taken as 0.075. If the formation is deeply invaded a value of 0.035 is preferred.

Water saturation can be applied to determine the fraction of pore volume occupied by formation water. If S_w approaches 1.0, the formation is completely saturated with water. Equation (1) and the resistivity relations have been incorporated into a chart by the Schlumberger Company [5] as shown in Fig. 3.1-15.

Porosity can be calculated from the following relation

$$\phi = \left(\frac{a}{F}\right)^{\frac{1}{m}} = \left(\frac{aR_w}{R_t S_w^2}\right)^{\frac{1}{m}} \qquad (2)$$

This formula was again proposed by Archie [5] where ϕ is fractional porosity and m and a are constants depending upon the type of formation.

For Hawaii, Keller [3] suggests that the constants in equation (2) are, a = 18 and m = 1.05. The relation is shown in chart form in Fig. 3.1-16. A sample calculation is helpful in illustrating the use of both charts.

The following resistivities were obtained at Kilauea Summit at a depth of about 1600 ft.

R_{mf} = 0.2 Ohm-meter
R_w = 0.08 "
R_i = 48.0
R_t = 80.0 "

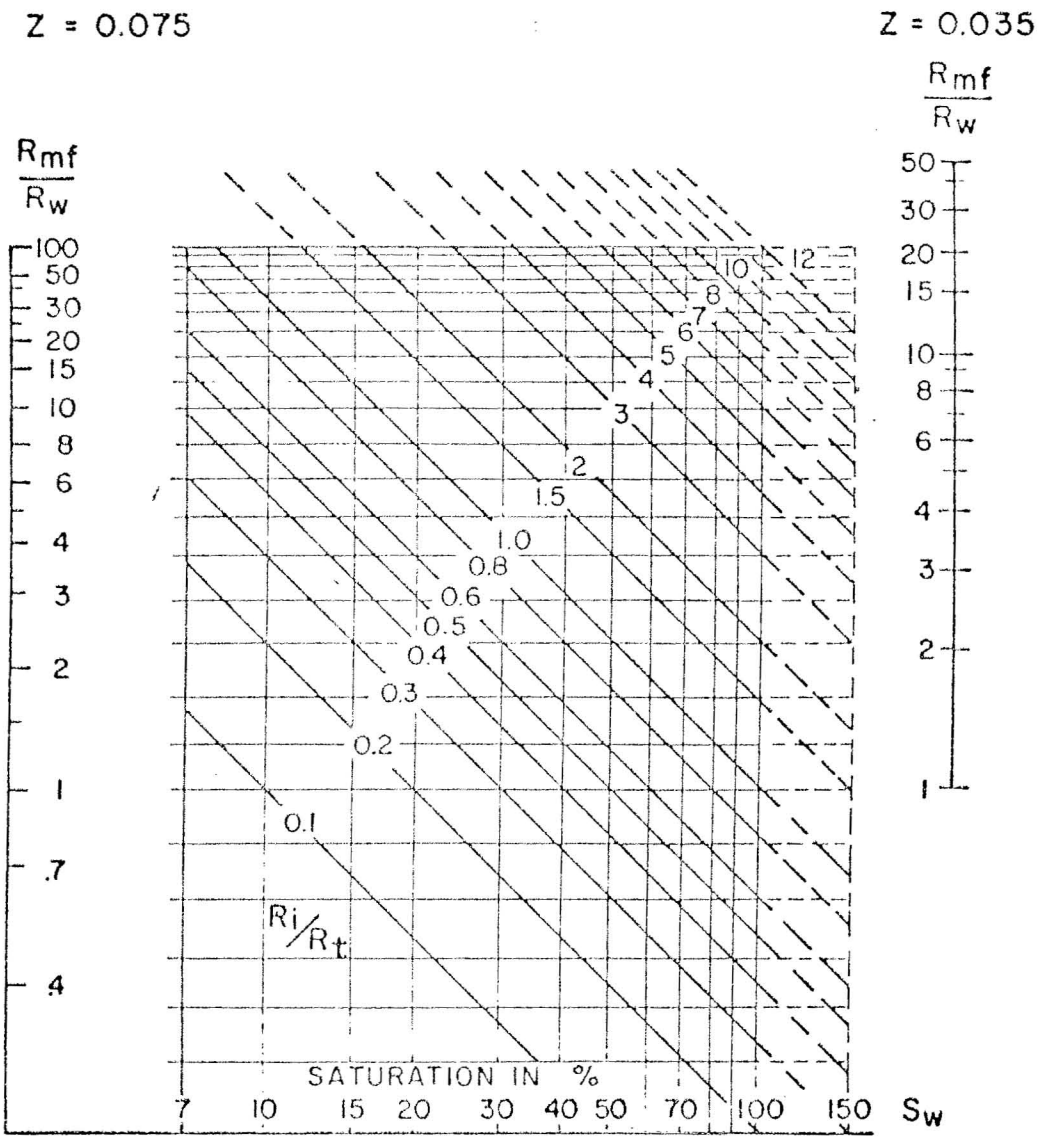

FIG. 3.1-15 RESISTIVITY RATIO CHART TO DETERMINE WATER SATURATION REF [5]

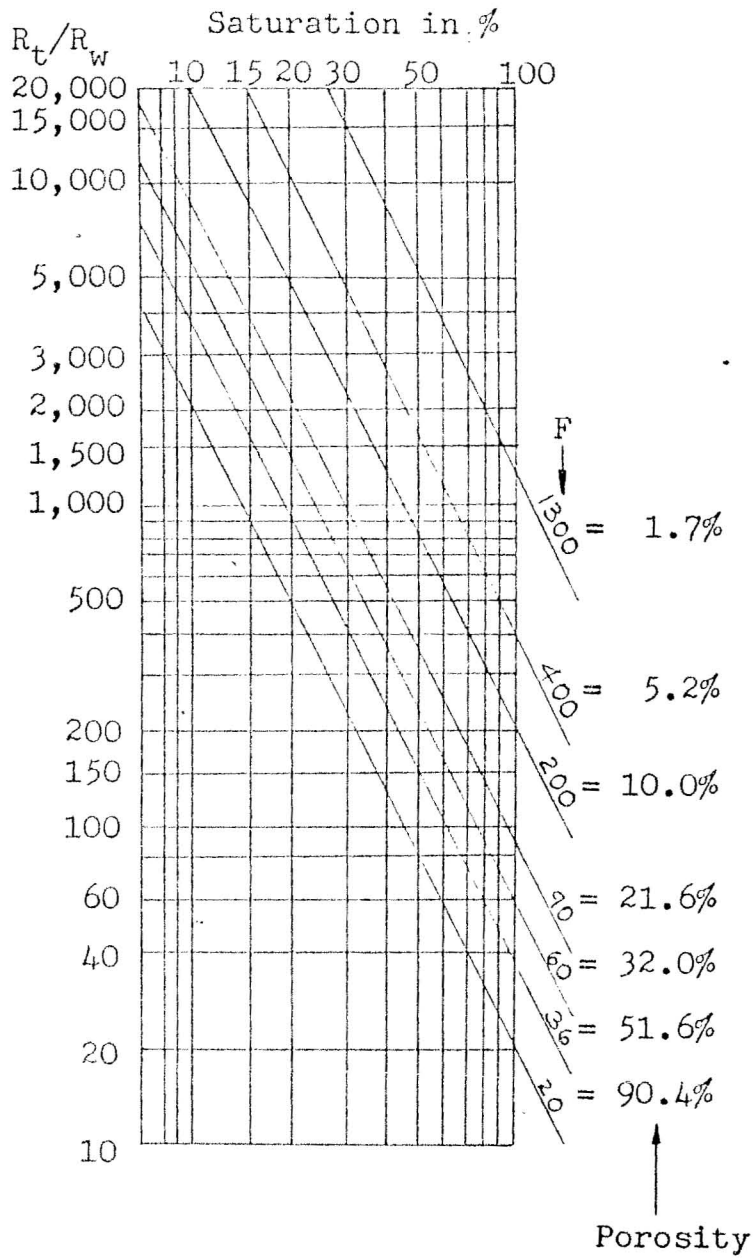

FIG. 3.1-16 POROSITY DETERMINATION FROM EMPIRICAL RELATIONS

Since mud infiltration was moderate, a Z value of 0.075 is assumed. Then R_i/R_t = 48.0/80.0 = 0.6 and R_{mf}/R_w = 0.2/0.08 = 2.5. From Fig. 3.1-15 S_w is approximately equal to 30%. Using this water saturation value and R_t/R_w = 80.0/0.08 = 1000, we obtain a porosity of 21.6% from Fig. 3.1-16.

This porosity can then be used in the following relation to obtain permeability

$$K = C\frac{\phi^x}{\left(\frac{c'}{\phi}\right)^y} \qquad (3)$$

In formations composed of sand, x and y are generally equal to 3.0 and 2.0, respectively. C is equal to 79 for gases and 250 for oils. Typically, the quantity $\left(\frac{c'}{\phi}\right)$ has a range of values from 1.0 to 0.50 depending upon c' at any given value of ϕ. This constant is influenced by the rock type and its grain size. Although permeabilities can be calculated by this relation, a greater accuracy is possible by performing a pressure drawdown test analysis during well production conditions.

Formation porosities are also obtainable by sonic and radioactive devices. For the sonic log the Wyllie formula [6] is

$$\phi_s = \frac{\Delta t_{log} - \Delta t_{ma}}{\Delta t_f - \Delta t_{ma}} \qquad (4)$$

The values of Δt_{ma} range from 40 to 70 sec/ft depending upon the type of formation. A typical value of Δt_f is 70 sec/ft while brines exhibit values in the neighborhood of 190 sec/ft. Since sonic logs measure primary porosities only, its range of values is usually low, between 2 to 10%.

The radioactive density log relation is similar to the sonic log. The empirical relation is

$$\phi_D = \frac{\rho_{ma} - \rho_b}{\rho_{ma} - \rho_f}$$

The density of matrix rocks, ρ_{ma}, is typically about 2.65 gms/cc and the fluid density ρ_f, for water is approximately 1.0. The measured density, ρ_b, then gives the value for total porosity ϕ_D. The difference in values

between total porosity and primary porosity is secondary porosity or fracture porosity. However, the commonly used parameter in reservoir analysis is total porosity.

In the Imperial Valley, porosities are greater than 25% in the production zone. Porosities at Kilauea Summit fluctuate from a low value of 2% to a high of 30% over the depth of the borehole. Well specialists suggest that porosities in the range of 20% to 30% are desirable in the production zone for adequate flow rates [6, 7].

In early logging the previously described analytical methods were done manually to obtain the desired subsurface information. However, with significant advances by well service companies, the process is now performed by applying computer programs for specific types of formations. The two common types of complete open-hole interpretation programs are the SARABAND and the CORIBAND techniques, both developed by the Schlumberger Company. SARABAND is applicable for shaley sands while CORIBAND is used primarily for complex lithologies.

b. Well Test Analysis

In order to evaluate a geothermal reservoir, whether it be drilling, development or production, various data on certain parameters are needed. These include formation thickness, permeability, porosity, viscosity, compressibility, thermal conductivity, fluid and rock density, temperature and formation average pressure.

Pressure is a particularly important parameter for use in materials heat balance calculations of geothermal liquid in place and determination of reservoir characteristics: compressed liquid, saturated liquid and steam or superheated steam. Finally, extrapolation into the future is best made by using the method which relates future production to future average pressure.

1) Mass Balance

$$W_c = W - W_p - W_L + W_e \qquad (5)$$

where W_c = current mass in reservoir, lbs.

W = initial mass in reservoir at the start of production, lbs.

W_p = mass produced, lbs.

W_L = mass lost via springs, wild wells, etc., lbs.

W_e = mass influx through aquifer, lbs.

2) Volumetric Balance

$$V\phi = (W - W_p - W_L + W_e)\ \left(x(v_g - v_f) + v_f\right) \qquad (6)$$

where V = reservoir bulk volume, ft^3

ϕ = porosity, fraction of bulk volume

x = steam quality in reservoir, mass fraction of fluid which is steam

v_g = specific volume of steam, ft^3/lb

v_f = specific volume of liquid water, ft^3/lb

3) Heat Balance

$$W_c h_c + (1 - \phi)\, V\rho_r C_r\, (T - T_o) = Wh_i + (1 - \phi)\, V\rho_r C_r\, (T_i - T_o)$$

$$- W_p h_p - W_L h_L + W_e h_e + Q_s \qquad (7)$$

where h_c = average enthalpy of total fluids in reservoir, btu/lb

h_i = average enthalpy of initial fluids in reservoir, btu/lb

h_p = average enthalpy of produced fluids, btu/lb

h_L = average enthalpy of lost fluids, btu/lb

h_e = average enthalpy of liquid water influx, btu/lb

ρ_r = formation density, lb/ft^3

C_r = specific heat of formation, btu/lb-F

T = current reservoir temperature, F

T_i = initial reservoir temperature, F

T_o = some reference temperature, F

Q_s = net heat conducted into reservoir, btu

The average enthalpy of any liquid-steam combination can be expressed by:

$$h = x(h_g - h_f) + h_f$$

where h = enthalpy of steam quality x, btu/lb

h_g = enthalpy of saturated steam, btu/lb

h_f = enthalpy of saturated liquid, btu/lb

Then with equations (5), (6), and (7) it is possible to solve for a set of unknowns (i.e., W--initial mass, T_i--initial temperature). The other parameters can be obtained through the production data or by estimations based on other geothermal wells.

In general, the well measurement program will obtain the average pressure of the reservoir vs. cummulative production in order to predict any future performance.

4) Background Material [3]

a) Dimensionless Equations

$$t_D = \frac{kt}{\phi \mu C_t r_w^2} \tag{8}$$

$$r_D = \frac{r}{r_w} \tag{9}$$

$$P_D = \frac{2\pi kh}{g\mu} (P_i - P_{r,t}) \tag{10}$$

where k = permeability, md
t = time, hr
ϕ = fractional porosity
μ = viscosity, cp
C_t = total system effective total isothermal compressibility, psi^{-1}
r_w = well radius, ft
r = distance from well, ft
h = formation net thickness, ft
g = production, std bbl/day
P_i = initial pressure, psi
$P_{r,t}$ = pressure at r ft, time t hrs, psi

b) Line Source Solution with Infinite Reservoir

Assumptions: (1) small pressure gradient
(2) fluid of small and constant compressibility
(3) rock properties are not functions of the angular direction or vertical coordinates

Solving with

initial condition: $p = p_D$ @ $t_D = 0$ for all r_D (11)

boundary condition: $\lim_{r_{D\to\infty}} P_D(r_D, t_D) = 0$

$$\lim_{r_D \to 0} \left(r_D \frac{dp_D}{dr_D}\right) = -1$$

$$P_D(r_D t_D) \approx \frac{1}{2}\left[\ln \frac{t_D}{r_D{}^2} + 0.80907\right] \quad (12)$$

where $\frac{t_D}{r_D{}^2} > 70$

Once we have the relationship between P_D and $t_D/r_D{}^2$, we can obtain the real pressure term $p_{r,t}$ at any location and time.

c) Interference Test

"Interference" means the production of one well causing a detectable pressure drop at an adjacent well. The most simple case of interference is when pressure drop is measured at a shut-in well.

To perform the interference test data analysis, the technique of type curve matching is developed.

$$\log_{10} p_D = \log_{10} \frac{2\pi kh}{9\mu} (p_i - p_{r,t})$$

$$= \log_{10} \left(\frac{2\pi kh}{9\mu}\right) + \log_{10} (p_i - p_{r,t}) \quad (13)$$

Then, the plot of p_D and $(p_i - p_{r,t})$ will be the same on log-log paper with the difference using a constant term. A plot of the logarithm of the real pressure differences must look exactly like a graph of the logarithm of p_D as long as the same size log cycle is used.

The procedure for the interference data analysis is as follows:

(1) Graph the pressure drop at the observation well vs. time.

(2) Position the field data curve over the type curve and move it keeping axes parallel until the field data matches the line source solution.

(3) Read a "match point" as the corresponding coordinates of any point common to both graphs, while aligned.

(4) From the pressure and time match we will be able to determine the values of two reservoir parameters (i.e., permeability and porosity).

d) Skin Effect

Physically, the skin effect is a combination of invasion by drilling fluids, dispersion of clays, presence of a mud cake and of cement, presence of condensation near a steam well, partial well penetration, limited perforation and even stimulation treatment such as acidization or hydraulic fracturing.

The skin effect may be positive, negative, or zero. If the well is damaged, s(skin effect) will be positive. If the well is stimulated, s will be negative. However, if the permeability in the skin zone is the same as in the rest of the formation, then s will be zero. Also note that skin effect comes into play only if one wants the pressure measured at or near a well.

e) Bounded Reservoir

Unfortunately no reservoirs are infinite in size and most large reservoirs have more than one well. Therefore, all wells more or less have a finite reservoir volume from which fluids are drained.

The drainage area of many wells tends to be more of a square or rectangular shape than circular.

Equation (12) can be expressed as

$$p_D(t_{DA}) = \frac{1}{2}\left[\ln\frac{4At_{DA}}{\gamma r_w^2}\right] \qquad (14)$$

$$t_{DA} = \frac{0.000264\ kt}{\phi\mu C_t A} = t_D\frac{r_w^2}{A}$$

γ = exponential of Euler's constant $\cong$ 1.781

At $t_{DA} \leq 0.05$, the effect of the boundaries is not felt at the well which behaves like a well in an infinite reservoir.

One notices that for a bounded reservoir, i.e., where no fluids cross the boundary, the dimensionless pressure increases rapidly as $t_{DA} \geq 0.1$. This obviously is due to the depletion of fluids throughout the reservoir. On the other hand for a constant pressure reservoir, the dimensionless pressure approaches a constant which is due to the replenishment of fluids through the boundary.

At steady-state, the dimensionless pressure at the well in the water of a constant pressure square is

$$p_D = \frac{1}{2} \ln \frac{16A}{\gamma C_A r_w^2} \quad , \quad t_{DA} \geq 0.25 \tag{15}$$

C_A = shape factor for a well in a closed square, 30.88

At pseudo steady-state, the linear equation for dimensionless pressure at the well in the center of a bounded square is

$$p_D = \frac{1}{2} \ln \left[\frac{4A}{\gamma C_A r_w^2} \right] + 2\pi t_{DA} \quad , \quad t_{DA} \geq 0.1 \tag{16}$$

Equations (15) and (16) are perfectly general equations for all different shapes of reservoirs and well locations, if the shape factor C_A can be determined.

f) Pressure Drawdown Test

A pressure drawdown test is a series of bottom-hole pressure measurements made during a period of constant producing rate flow. Prior to the flow test, the well is usually shut-in to allow the pressure to be equalized throughout the formation. Drawdown tests are normally run on new wells or after a well has been shut-in for a long period.

The following is a summary of the drawdown test analysis procedure.

(1) Plot p_{wf} (bottom-hole flowing pressure) vs. $\log_{10} t$, find correct semilog straight line, slope, m and p_{1hr}. It may at times appear to have more than one possibility for a straight line. Suggested procedure is to plot $(p_i - p_{wf})$ vs. t on log-log type paper and compare with the line source solution type curve to determine the onset of the correct straight line.

(2) Find k, s, Δp_{skin} (real pressure drop due to skin effect) and FE (flow efficiency) with the appropriate equations.

g) Pressure Buildup Test

The pressure buildup test is the most important well test in reservoir engineering because it yields a great deal of information, such as, permeability, skin effect, and, perhaps most important of all, the static average pressure in the drainage area with respect to the Matthew-Brons-Hazeboek function.

$$p_{D_{MBH}} = \frac{bh}{70.65 g \mu \beta} (p^* - \bar{p})$$

$$= 4\pi t_{DA} - 2p_D(t_D) + \left[\ln t_D + 0.80907\right] \qquad (17)$$

p^* (false pressure) is the pressure extrapolated to infinite shut-in time.

$$p_{D_{MBH}} = \ln\left(\frac{t + \Delta t}{\Delta t}\right) p_{ws} = \bar{p} \qquad (18)$$

Then from plots of $p_{D_{MBH}}$ vs. Δt_{DA} (Mathew-Brons-Hazebroek Function) for various drainage shapes one can get the average pressure.

The following is a summary of pressure buildup analysis by the Horner graph method:

(1) Plot p_{ws} (downhole well static pressure) vs. $\log_{10}\left(\frac{t+\Delta t}{\Delta t}\right)$, find m (slope), p_{1hr}, p^* at $\frac{t+\Delta t}{\Delta t} = 1$. At times it may seem to have more than one possibility for a straight line. The suggested procedure is to plot $(p_{ws} - p_{wf})$ vs. Δt on log-log type paper and compare with the line source solution type curve to determine the onset of the correct straight line.

(2) Calculate k, s, Δp_{skin}, and FE with the appropriate equations.

(3) For $\bar{p}$:

(a) Calculate t_{DA}, the dimensionless produced time.

(b) Determine the drainage shape and well location.

(c) Find $\bar{p}$ by going to a MBH pressure function plot.

c. Physical Modelling [2, 8-13]

A portion of a geothermal reservoir will be modelled to determine the feasibility of using a physical model for predictive purposes. The model will also be used to confirm computer predictions. To insure similarity between the physical and mathematical models and an actual reservoir, a modified Rayleigh number will be used. This dimensionless number is defined as follows:

$$\text{mod Ra} = \text{Ra}\,\frac{k}{L^2}$$

where Ra = Rayleigh No.
k = permeability
L = characteristic length

since $$Ra = \frac{\beta g \Delta T L^3}{\alpha \nu} ,$$

$$\text{mod } Ra = \frac{\beta g \Delta T L K}{\alpha \nu}$$

where β = coefficient of thermal expansion
α = thermal diffusivity
ν = kinematic viscosity
g = gravitational constant
ΔT = difference in temperature between the reservoir and ocean
L = height of aquifer

Convection is initiated at a modified Rayleigh number of 40; mod Ra's up to 1,000,000 can be expected for actual conditions in Hawaii. Calculations showed that it is possible to obtain mod Ra's up to 1,000 using the full scale unpressurized model (see Table 3.1-1). This model is tentatively planned to have a seawater capacity of 450 gallons, a variable (in size and temperature) heat source and glass bead permeable medium. As the model will be two-dimensional, one face will be used to insert temperature measurement devices to obtain the temperature profile.

Three glass bead mesh sizes will be used to vary permeability (see Table 3.1-2). Various researchers have speculated that macroscopic fractures will result in aquifer permeabilities in the order of several hundred darcies. It was fortuitous that glass bead permeabilities were available to straddle this range and yet provide for reasonably high modified Ra numbers. Glass beads having mesh size/permeability of 12-14/1490, 20-30/319, and 40-50/80 were selected. Lower permeabilities can be obtained by using higher mesh sizes, consolidation, or artificial dike formation.

A preliminary 50 gallon (1/3 size) model will be initially built. This smaller tank will give an economical means of testing construction and operational costs. Certain design questions such as to pressurize or unpressurize will also be answered. The heat source and temperature measurement and recording instruments will be the same for both the preliminary and final models. Materials and equipment for the preliminary model have been ordered and fabrication has commenced.

TABLE 3.1-1

MODIFIED RAYLEIGH NUMBERS FOR
VARIOUS MODEL SIZES AT
DIFFERENT EXPERIMENTAL ΔT's

ΔT, °F	Full Size	1/2 Size	1/3 Size	1/4 Size
10	46.9	23.5	15.6	11.7
20	93.8	46.9	31.2	23.5
30	140.7	70.4	46.8	35.2
40	187.6	93.9	62.4	46.9
50	234.5	117.4	78.0	58.7
60	281.4	140.9	94.0	70.4
70	328.3	164.4	109.0	82.1
80	375.2	187.9	125.0	93.8
90	422.1	211.4	140.0	106.0
100	469.0	234.9	156.0	117.0
200	938.0	469.0	312.0	234.0
300	1407.0	704.0	468.0	351.0
400	1876.0	938.0	624.0	468.0

Porous medium: 12-14 mesh glass beads

Fluid medium: seawater

TABLE 3.1-2

CALCULATED PERMEABILITIES OF GLASS BEADS

Mesh Size	Size Range (inches)	Size Range (microns)	Average Size (microns)	Permeability (cm^2)	Darcy
12 - 14	0.0661 - 0.0555	1680 - 1410	1545.0	1.47×10^{-5}	1490
14 - 20	0.0555 - 0.0331	1410 - 840	1125.0	7.81×10^{-6}	792
20 - 30	0.0331 - 0.0232	840 - 590	715.0	3.15×10^{-6}	319
30 - 40	0.0232 - 0.0165	590 - 420	505.0	1.57×10^{-6}	159
40 - 50	0.0165 - 0.0177	420 - 297	358.5	7.93×10^{-7}	80
50 - 70	0.0177 - 0.0083	297 - 210	253.5	3.97×10^{-7}	40
140 - 230	0.0041 - 0.0024	105 - 62	83.5	4.30×10^{-8}	4

C. Future Work

1. Numerical Modelling of Geothermal Reservoirs

During the next quarter, both the numerical solutions for free convection at large Rayleigh numbers in confined geothermal reservoirs as well as for steady withdrawal and reinjection of fluids in confined geothermal reservoirs will be extended to unconfined reservoirs. The numerical solution for the dynamics of the Ghyben-Herzberg lens will be continued.

2. Well Test Analysis and Physical Modelling

Although on the one hand there are several methods and assorted equipment available for geothermal well testing, the relative newness of the field has resulted in a less than satisfactory hardware and software availability situation. Table 3.1-3 lists the hardware and the tested parameter for Test Well Mesa in the Imperial Valley and for the test hole at Kilauea Summit. Although there are other elaborate logging techniques, the common types are those listed in this table.

The selection of a particular fluid testing device will depend on equipment durability, accuracy, measuring limits and cost. The Amerada-Kuster wireline gauges seem to best fulfill requirements with relatively high accuracy and measuring limits at a cost as low as one tenth that of electronic devices.

Formation logging tests will probably be contracted out to a well service company. If tests on several wells are anticipated, it is recommended that a set of Amerada-Kuster gauges with their hoist equipment be purchased. Thus, future work will consist of purchasing the equipment and familiarizing task personnel with calibration and utilization techniques.

Coordination must be continued with the geophysical drilling program to insure that measurement equipment, both downhole and at wellhead, be provided for in the budget. The contract for the initial measurement must also be jointly settled.

The future software study will consist of developing computer programs to predict well and reservoir performance [14-16]. The time available for prediction will be strategic. Accuracy should be satisfactory if one year is allowed for measurement and analysis. Various

TABLE 3.1-3

COMPARISON OF WELL TEST METHODS

Hardware and Method		Measured Parameter
Hawaii	Imperial Valley	
1. Spontaneous Potential (SP) 2. Induction Log (IL) 3. Lateral Log (LL)	1. Dual Induction Laterol Log (combination of SP, IL & LL)	Formation Resistivities
1. Sonic 2. Gamma Density 3. Neutron Density	1. Sonic 2. Gamma Density 3. Neutron Density	Formation Porosities
1. Thermistor Probe 2. Maximum Registering Mercury Thermometer 3. Wireline RTG Temperature Gage (Kuster)	1. Maximum Registering Mercury Thermometer 2. Wireline Amerada RTG Gage	Formation Temperature
1. Wireline RPG Pressure Gage	1. Wireline Amerada RPG Gage	Formation Pressure

prediction techniques must, however, be developed for six months, two months, one month, two weeks, one day, and immediate prognostications.

Construction of the preliminary model will be completed by the end of January, 1975. The rest of the timetable was indicated earlier. An important date is April 30, 1975, when the design of the large model will be decided after analysis of the data from the preliminary model. Comparisons between the physical and computer models will be made periodically.

D. References

1. Lau, K.H. & P. Cheng, "The Effect of Dike Intrusion on Free Convection in a Geothermal Reservoir," Tech. Rept. No. 7, Hawaii Geothermal Project, December 1, 1974.

2. Cheng, P. & K.H. Lau, "Steady State Free Convection in an Unconfined Geothermal Reservoir," *J. of Geophysical Research*, V. 79, No. 29, 1974, pp. 4425-4431.

3. Keller, George V., "Drilling at the Summit of Kilauea Volcano," Prepared for NSF, Colorado School of Mines, March, 1974.

4. Greenspan, D., "Numerical Studies of Viscous, Incompressible Flow Through an Orifice for Arbitrary Reynolds Number," *Int. J. for Numerical Methods in Engineering*, V. 6, 1973, pp. 489-496.

5. Schlumberger, *Log Interpretation Volume II - Applications*, Schlumberger, Ltd., New York, 1974.

6. Schlumberger, *Log Interpretation Volume I - Principles*, Schlumberger, Ltd., New York, 1972.

7. Armstrong, E.L. and E.A. Lundberg, "Geothermal Resource Investigations Test Well Mesa 6-1," February, 1973.

8. Bear, Jacob, *Dynamics of Fluids in Porous Media*, American Elsevier Publishing Company, Inc., New York, 1972.

9. Elder, John W., "Physical Processes in Geothermal Areas," *Terrestrial Heat Flow*, W.H.K. Lee, Editor, No. 8, 1965, pp. 211-239.

10. Furumoto, Augustine S., "U.S.-Japan Seminar on Utilization of Volcanic Energy," Summary of Proceedings of Seminar, February 4-8, 1974.

11. Henry, H.R. and F.A. Kohout, "Circulation Patterns of Saline Groundwater Affected by Geothermal Heating--as Related to Waste Disposal," *Underground Wastewater Management and Environmental Implications*, Vol. 18, 1973, pp. 202-221.

12. Wooding, R.A., "Convection in a Saturated Porous Medium at Large Rayleigh Number or Peclet Number," *Journal Fluid Mechanics*, Vol. 15, 1963, pp. 527-544.

13. Wooding, R. A., "Rayleigh Instability of a Thermal Boundary Layer in Flow Through a Porous Medium," *Journal Fluid Mechanics*, Vol. 9, 1960b, pp. 183-192.

14. Ramey, H.J., Jr., *Gas Well Test Analysis Under Water-Drive Conditions*, A.G.A., 1973.

15. Ramey, H.J., Jr., "A Reservoir Engineering Study of the Geysers Geothermal Field," *Private Correspondence*, 1973.

16. Russell, D.G. and C.S. Matthews, *Pressure Buildup and Flow Tests in Wells*, S.P.E., 1967.

TASK 3.6 OPTIMAL GEOTHERMAL PLANT DESIGN

Investigators: H. C. Chai, J. Chou, and D. Kihara

A. Timetable

December 31, 1974	1. Survey availability of components to be used with each working fluid 2. Construct components and assemble experimental heat transfer loop
June 30, 1975	1. Establish general requirements, ground rules, and design criteria for a research-oriented plant for liquid-dominated fields 2. Construct and test horizontal heat exchanger
December 31, 1975	1. Set up procedures for the design and selection of the components of regenerative binary fluid plants 2. Continue testing of horizontal heat exchanger and write computer program for horizontal heat exchanger 3. Begin testing of vertical heat exchanger
June 30, 1976	1. Lay out detailed flow diagrams of the plant based on a regenerative binary fluid system, with a vapor flashing system as the alternative 2. Analyze test data for horizontal heat exchanger and continue testing of vertical heat exchanger
December 31, 1976	1. Estimate capital costs of the plant, evaluate unit operating cost, and compare feasibilities of the two systems 2. Complete testing and analyze test data for vertical heat exchanger

TASK 3.6 OPTIMAL GEOTHERMAL PLANT DESIGN

B. Progress to Date

During the past quarter, work has been concentrated on establishing a technical basis on which a selection can be made between the vapor flashing system and the binary fluid cycle.

For the vapor flashing system, the effect of wellhead conditions on a particular hypothetical plant was studied. The hypothetical plant consists of a two-stage separator, a turbine with an efficiency of 73%, connected to the wellhead through a pipeline having a pressure drop of 10 psi and condensation loss of 3% of the heat content of the water. Assuming a well flow rate of one million pounds per hour of water with 3000 lb/hr of gases, the specific power output is shown in Fig. 3.6-1 as wellhead pressure and enthalpy are varied. It is to be noted that broad maxima of sorts exist for various wellhead conditions, e.g., for a wellhead enthalpy of 400 BTU/lb., maximum power output is obtained at roughly 80 psig wellhead pressure. Figures such as this can be used to compare the power production of a vapor flashing system against that of a binary fluid cycle system using the same wellhead conditions.

For the binary fluid cycle, the in-depth study of the cycle using isobutane is continuing. The basic cycle is assumed to be operating under the following representative conditions:

Brine temperature	350°F
Condenser outlet conditions	Saturated liquid at 100°F
Pinch point temperature difference	20°F
Pump efficiency	75%
Turbine efficiency	85%
Net power output	10 MW(t)

The effect of using system pressures greater than the critical pressure is shown in Figs. 3.6-2 to 3.6-4. Figs. 3.6-2 and 3.6-3 show the effect of system pressure and turbine inlet temperature on the thermal efficiency of the basic cycle and on the rate of consumption of the primary resource, brine. In general, higher system pressures lead to a reduced brine mass flow rate, although a minimum does appear to exist for a system pressure of 700 psia and turbine inlet temperature of 300°F (see Fig. 3.6-4).

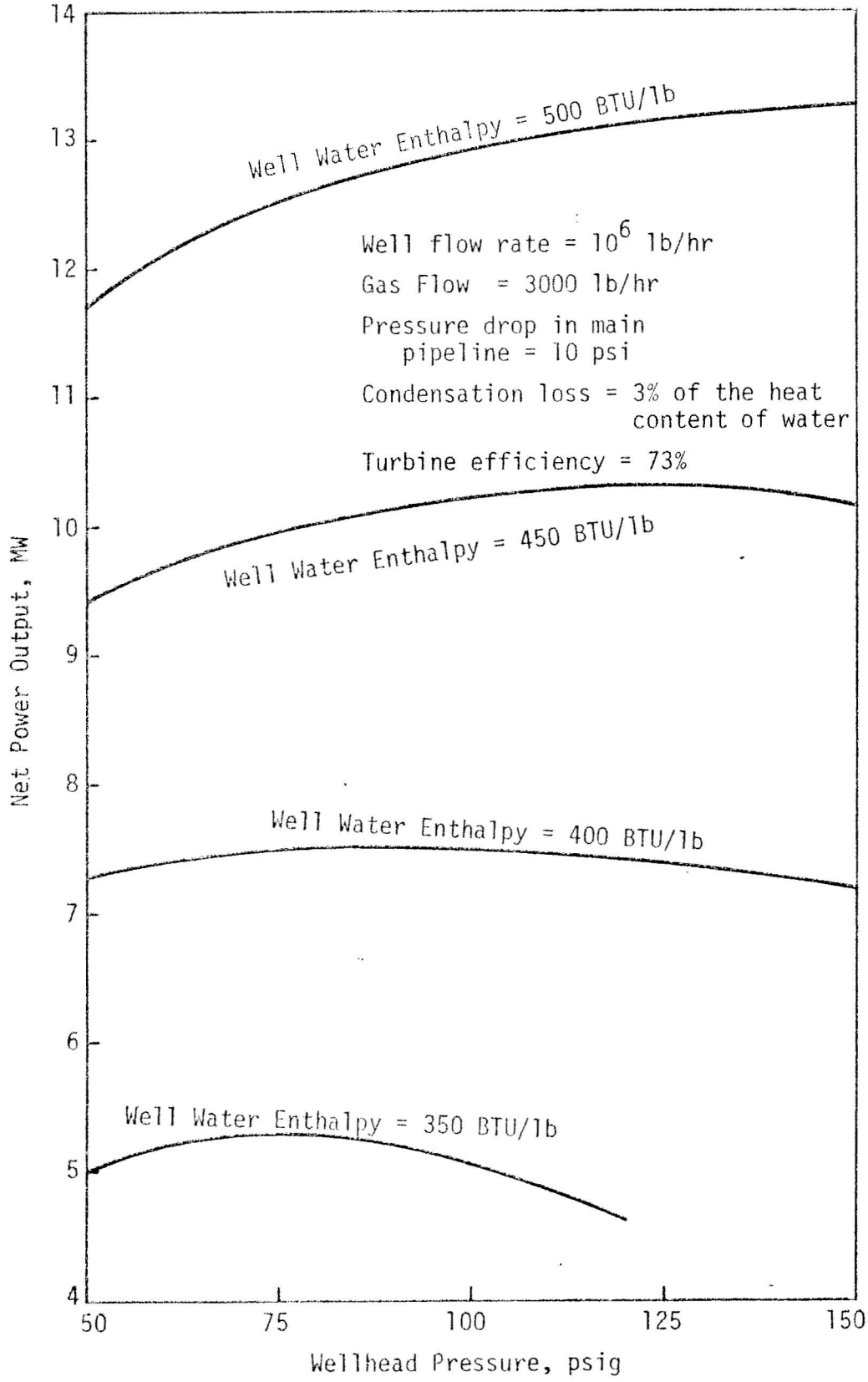

FIG. 3.6-1 VARIATION OF SPECIFIC POWER OUTPUT WITH WELLHEAD PRESSURE FOR A TWO-STAGE VAPOR FLASHING PLANT

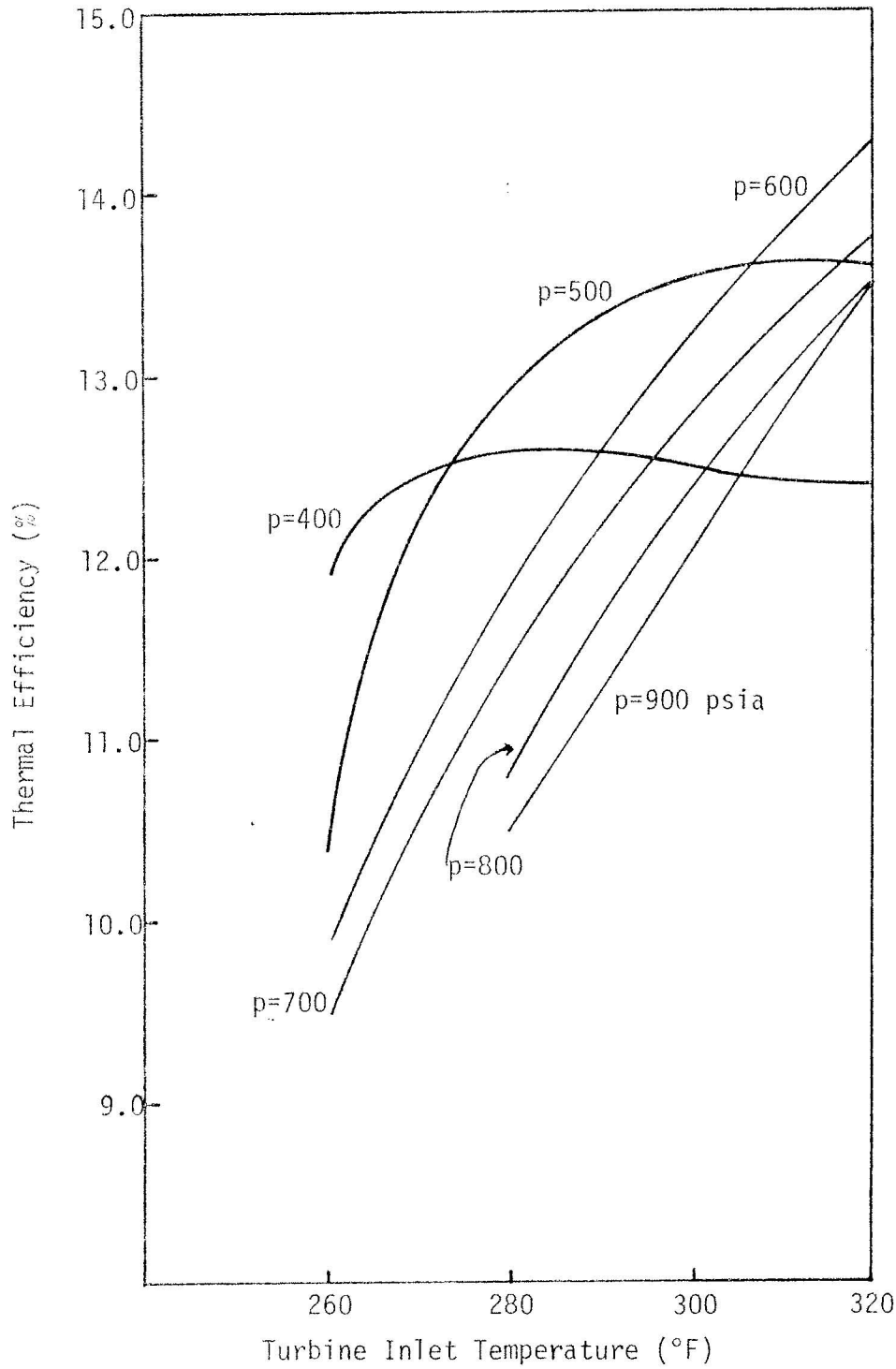

FIG. 3.6-2 THERMAL EFFICIENCY FOR ISOBUTANE CYCLE AS A FUNCTION OF TURBINE INLET TEMPERATURE AND SYSTEM PRESSURE

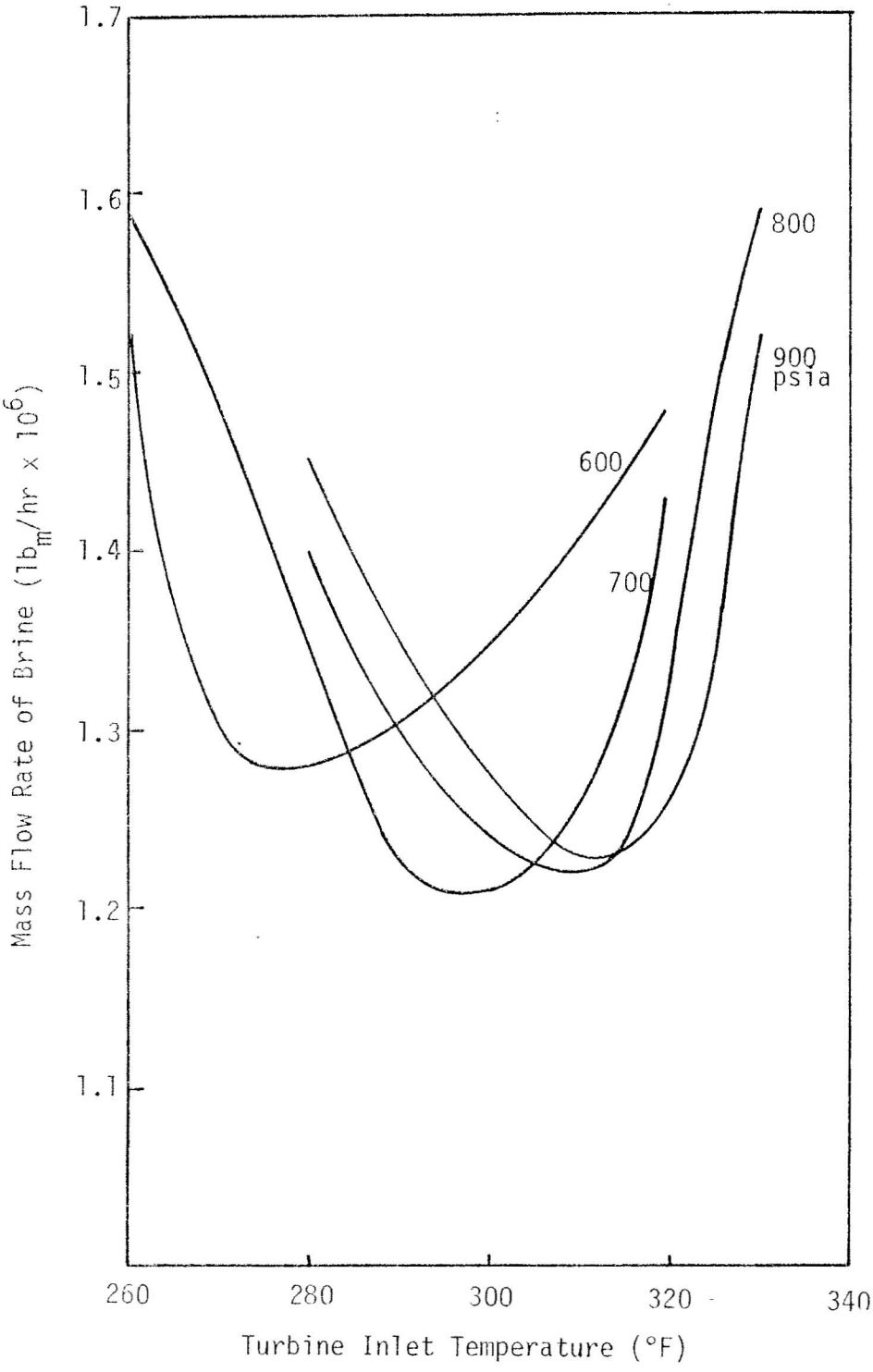

FIG. 3.6-3 BRINE FLOW RATE REQUIRED AS A FUNCTION OF TURBINE INLET TEMPERATURE FOR SUPERCRITICAL PRESSURES

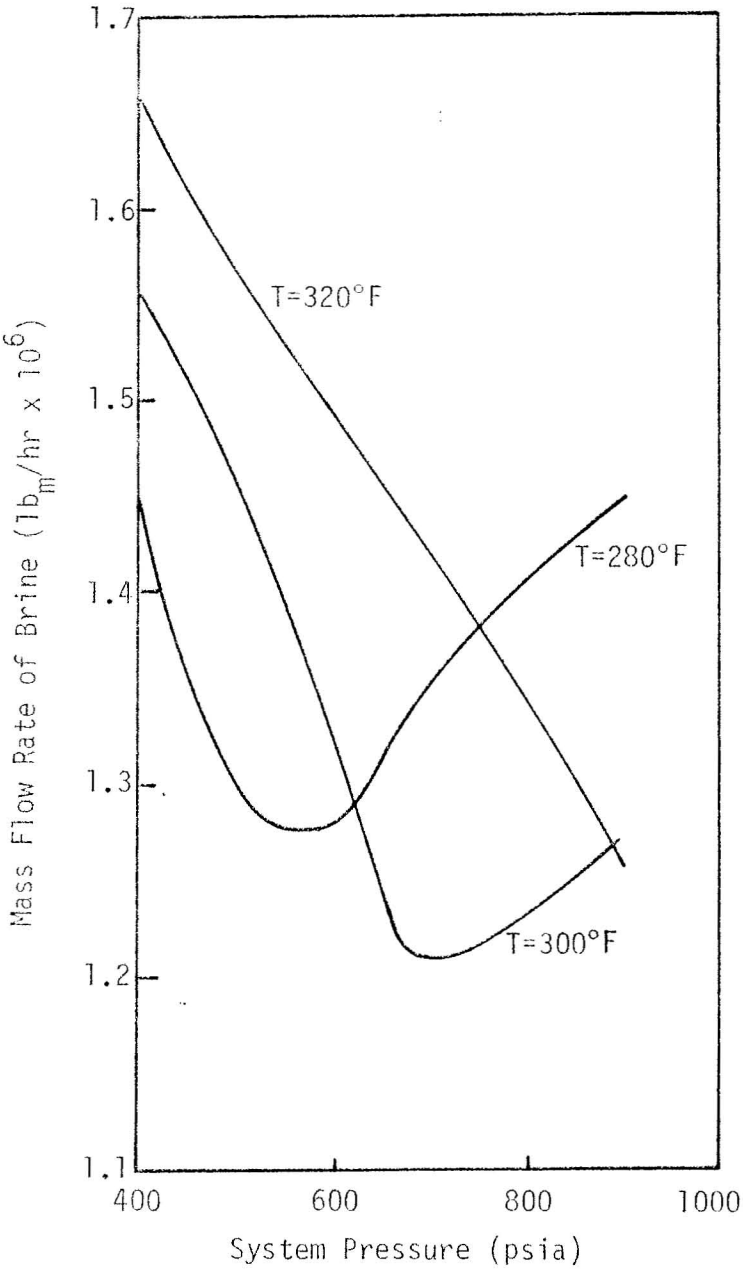

FIG. 3.6-4 BRINE FLOW RATE AS A FUNCTION OF SYSTEM PRESSURE

In addition to this in-depth study of a single working fluid, an exhaustive search of a broad range of possible working fluids is being conducted. The preliminary list of those candidate fluids being considered is listed in Table 3.6-1. To narrow this list to a workable number, a series of go-no go tests will be applied, e.g., thermal stability at 300°F. These will then be followed by a series of more detailed analyses related to the Rankine power cycle.

A survey of the availability of components for the binary fluid cycle power plant is in progress.

Construction of the experimental heat transfer loop is continuing.

TABLE 3.6-1

WORKING FLUIDS AND PROPERTIES

	Fluid	Chemical Formula	Molecular Weight	Critical Point	
				T_c °F	P_c psia
1.	Methane	CH_4	16.04	-116.00	673.0
2.	Ethane	C_2H_6	30.07	90.32	709.8
3.	Propane	C_3H_8	44.09	206.00	617.0
4.	n-Butane	C_4H_{10}	58.10	305.62	550.7
5.	Ethylene	C_2H_4	28.05	49.82	742.1
6.	Propylene	C_3H_6	42.08	197.40	667.0
7.	1-Butene	C_4H_8	56.10	295.60	583.0
8.	Cis-2-Butene	C_4H_8	56.10	324.30	600.0
9.	Trans-2-Butene	C_4H_8	56.10	311.90	600.0
10.	Propadiene (Allene)	C_3H_4	40.06	248.00	793.0
11.	1,3 Butadiene	C_4H_6	54.09	306.00	628.0
12.	1,2 Butadiene	C_4H_6	54.09	339.00	653.0
13.	Methyl Chloride	CH_3Cl	50.50	290.20	964.0
14.	Methylene Chloride	CH_2Cl_2	84.90	472.40	893.0
15.	Chloroform	$CHCl_3$	119.40	499.40	805.0
16.	Carbon Tetrachloride	CCl_4	153.80	541.00	660.0
17.	Vinyl Chloride	C_2H_3Cl	62.50	313.10	809.0
18.	Vinylidene Chloride	CH_2CCl_2	96.95	429.20	758.0
19.	Trichloroethylene	C_2HCl_3	131.40	567.80	710.0
20.	Perchloroethylene	C_2Cl_4	165.80	643.40	650.0

TABLE 3.6-1 (continued)

	Fluid	Chemical Formula	Molecular Weight	Critical Point	
				T_c °F	P_c psia
21.	Ethyl Chloride	C_2H_5Cl	64.50	368.00	761.0
22.	Ethylene Dichloride	$C_2H_4Cl_2$	99.00	553.40	780.0
23.	Propyl Chloride	C_2H_7Cl	78.50	445.40	663.0
24.	Propylene Dichloride	$C_3H_6Cl_2$	113.00	578.60	641.0
25.	Methanol	CH_4O	32.04	463.40	1155.0
26.	Ethanol	C_2H_6O	46.07	469.00	924.0
27.	Propanol	C_3H_8O	60.10	506.00	749.0
28.	Butanol	$C_4H_{10}O$	74.1	553.00	640.0
29.	Isopropyl Alcohol	C_3H_8O	60.10	454.90	691.0
30.	Isobutyl Alcohol	$C_4H_{10}O$	74.10	530.00	623.0
31.	Sec-butyl Alcohol	$C_4H_{10}O$	74.10	504.80	608.0
32.	Tert-butyl Alcohol	$C_4H_{10}O$	74.10	454.40	614.0
33.	Allyl Alcohol	C_3H_6O	58.08	521.00	831.0
34.	1-Amyl Alcohol	$C_5H_{12}O$	88.10	590.70	557.0
35.	1-Hexyl Alcohol	$C_6H_{14}O$	102.20	595.70	490.0
36.	1-Heptyl Alcohol	$C_7H_{16}O$	116.20	630.80	436.0
37.	Ethylene Oxide	C_2H_4O	44.10	383.80	1043.0
38.	Propylene Oxide	C_3H_6O	58.10	407.60	714.0
39.	Epichlorohydrine	C_3H_5OCl	92.50	612.80	721.0
40.	1,2 Butylene Oxide	C_4H_8O	72.10	468.80	630.0
41.	Ethylene Glycol	$C_2H_6O_2$	62.1	704.60	1120.0
42.	Diethylene Glycol	$C_4H_{10}O_3$	106.10	764.00	680.0

TABLE 3.6-1 (continued)

	Fluid	Chemical Formula	Molecular Weight	Critical Point	
				T_c °F	P_c psia
43.	Triethylene Glycol	$C_6H_{14}O_4$	150.20	818.00	486.0
44.	n-Pentane	C_5H_{12}	72.20	385.50	489.5
45.	n-Hexane	C_6H_{14}	86.20	454.10	440.0
46.	n-Heptane	C_7H_{16}	100.20	512.62	396.8
47.	n-Octane	C_8H_{18}	114.20	563.70	362.1
48.	1-Pentene	C_5H_{10}	70.13	376.90	586.0
49.	1-Hexene	C_6H_{12}	84.20	460.00	471.7
50.	1-Heptene	C_7H_{14}	98.20	507.40	426.2
51.	1-Octene	C_8H_{16}	112.20	560.30	395.3
52.	Isobutane	C_4H_{10}	58.12	274.96	529.1
53.	Isobutylene	C_4H_8	56.10	291.90	580.0
54.	Isoprene	C_5H_8	68.11	412.00	558.4
55.	Isopentane	C_5H_{12}	72.20	369.00	483.0
56.	Isohexane	C_6H_{14}	86.17	435.10	440.0
57.	2-Methylhexane	C_7H_{16}	100.20	495.00	400.0
58.	Isooctane	C_8H_{18}	114.20	519.40	375.0
59.	2-Methylheptane	C_8H_{18}	114.20	547.50	364.0
60.	Formaldehyde	CH_2O	30.02	278.00	984.0
61.	Acetaldehyde	C_2H_4O	44.05	369.80	803.0
62.	Propionaldehyde	C_3H_6O	58.08	427.40	674.0
63.	Butylaldehyde	C_4H_8O	72.11	477.80	580.0
64.	Acetone	C_3H_6O	58.08	454.40	690.0

TABLE 3.6-1 (continued)

	Fluid	Chemical Formula	Molecular Weight	Critical Point	
				T_c °F	P_c psia
65.	2-Butanone	C_4H_8O	72.10	503.90	602.0
66.	3-Pentanone	$C_5H_{10}O$	86.13	599.40	542.0
67.	4-Methylpentanone-2	$C_6H_{12}O$	100.16	568.30	475.0
68.	Methyl Ether	C_2H_6O	46.07	259.80	763.0
69.	Ethyl Ether	$C_4H_{10}O$	74.12	380.20	522.0
70.	Propyl Ether	$C_6H_{14}O$	102.20	488.60	414.0
71.	Butyl Ether	$C_8H_{18}O$	130.20	584.00	345.0
72.	Methyl Acetate	$C_3H_6O_2$	74.08	452.10	666.0
73.	Ethyl Acetate	$C_4H_8O_2$	88.10	481.60	557.0
74.	Butyl Acetate	$C_6H_{12}O$	116.16	582.20	442.0
75.	Vinyl Acetate	$C_4H_6O_2$	86.10	485.00	609.0
76.	Acetic Anhydride	$C_4H_6O_3$	102.09	564.20	675.0
77.	Propionic Anhydride	$C_6H_{10}O_3$	130.15	594.80	478.0
78.	Ethyl Formate	$C_3H_6O_2$	74.09	454.90	686.0
79.	Isopropyl Acetate	$C_5H_{10}O_2$	102.15	468.80	507.0
80.	Benzene	C_6H_6	78.11	552.00	714.0
81.	Ethylbenzene	C_8H_{10}	106.16	651.20	540.0
82.	Propylbenzene	C_9H_{12}	120.19	689.40	460.0
83.	Cumene	C_9H_{12}	120.19	676.20	460.0
84.	Cyclopropane	C_3H_6	42.08	256.00	797.0
85.	Cyclobutane	C_4H_8	56.10	373.40	713.0
86.	Cyclopentane	C_5H_{10}	70.13	461.48	654.7

TABLE 3.6-1 (continued)

	Fluid	Chemical Formula	Molecular Weight	Critical Point	
				T_c °F	P_c psia
87.	Cyclohexane	C_6H_{12}	84.16	535.60	591.5
88.	Bromobenzene	C_6H_5Br	157.02	746.00	655.0
89.	Chlorobenzene	C_6H_5Cl	112.56	678.00	655.0
90.	Fluorobenzene	C_6H_5F	96.10	547.30	655.0
91.	R-11	CCl_3F	137.38	388.40	640.0
92.	R-12	CCl_2F_2	120.93	233.60	597.0
93.	R-22	$CHClF_2$	86.48	204.80	721.9
94.	R-113	$CCl_2F-CClF_2$	187.39	417.40	498.9
95.	R-114	$C_2Cl\ F_4$	170.94	294.30	473.0
96.	R-115	CF_3CF_2Cl	154.50	175.90	458.0
97.	R-502	$CHClF_2$ (48.8%) $CClF_2CF_3$ (51.2%)	111.60	194.00	619.0
98.	R-318	C_4F_8	200.04	239.60	403.6
99.	R-13B1	$CBrF_3$	148.93	152.60	575.0

C. Future Work

During the next quarterly period, the following work will be undertaken:

1. Survey of availability of components which can be used in a regenerative binary fluid cycle power plant will be continued.
2. Construction of components will continue and assembly and check-out of experimental heat transfer loop will be continued.
3. Broad criteria for selecting from the list of candidate working fluids will be compiled.